

# Fully Vectorized Linear Operator Formulation for Inverse Scattering Problems

Version 1.02

Msc Physics ETHZ

Submitted by Richard Gengo Wueest

## **Advisors:**

Dr. Henrik Rasmus Thomsen

Dr. Johannes Aichele

Jonas Mueller

Dr. Prof. Johan Robertsson

## **Abstract**

This thesis introduces a fully vectorized linear operator framework for inverse scattering problems in non-destructive testing (NDT) of composite structures. The method is model-free, relying on empirically measured impulse responses and Tikhonov regularization from a linear time-invariant (LTI) system perspective, rather than traditional analytical wave models. Simulations on aluminium plates demonstrate that the approach achieves strong noise robustness, supports flexible sensor configurations, is computationally efficient, and is capable of sub-wavelength localization. The methodology is broadly applicable to flat objects made of complex, anisotropic materials with arbitrary shape and curvature.

## Acknowledgement

I would like to thank my advisor, Dr. Henrik Rasmus Thomsen, for his support in helping me develop this thesis. This work began as a collection of loosely connected ideas, which gradually developed into a formal proposal in the form of a semester project, subsequently leading to the present thesis. In its early stages, the project barely resembled the final outcome and required a great deal of trust from Henrik to let it develop organically into its present form.

Our differing perspectives, due to originating in different fields of study, led to valuable exchanges on problem-solving approaches. I believe that such interdisciplinary cooperation, and the opportunity for students to independently explore their ideas, represents academia at its best.

I hope this spirit of collaboration becomes more common.

# Contents

<b>1</b>	<b>Introduction</b>	<b>5</b>
1.1	Terminology . . . . .	5
1.2	Ultrasonic NDT: Context and Motivation . . . . .	5
1.3	Summary of Contributions and Key Results . . . . .	6
1.4	Mathematical Framework (without derivation) . . . . .	7
1.5	The Thesis in Context . . . . .	8
1.5.1	Vectorization and Linear Algebraic Approach . . . . .	9
1.5.2	Empirical and Analytical Models . . . . .	9
1.5.3	Relation to Digital Twins and Waveform Inversion . . . . .	9
1.5.4	Industry Standard: Echo-Based and C-Scan Methods . . . . .	10
1.6	Thesis objective . . . . .	10
<b>2</b>	<b>Mathematical derivation</b>	<b>10</b>
2.1	Modeling Assumptions . . . . .	10
2.2	On periodic time . . . . .	11
2.3	Behavior of a Linear quantity inside a time invariant object . . . . .	11
2.4	The generalized linear quantity . . . . .	12
2.5	Behavior of Defects . . . . .	12
2.6	System Matrix Assembly . . . . .	13
2.7	Generalizing the Defect Space . . . . .	15
2.8	Impulse Response Construction using Tikhonov Regularization . . . . .	16
2.9	Regularized Inverse Problem and Tikhonov Solution . . . . .	19
2.10	Modified Regularization Matrix for Transducer Self-Correction . . . . .	19
2.11	Explicit System Configurations . . . . .	20
2.12	Algorithm Summary . . . . .	21
<b>3</b>	<b>Methodology</b>	<b>21</b>
3.1	General Structure and Data Handling . . . . .	21
3.2	Simulation, Raw Data, and Visualization . . . . .	22
3.3	Impulse Response Calculation and Visualization . . . . .	24
3.4	System Matrix Assembly and Inversion . . . . .	25
3.5	Defect Evaluation and Visualization . . . . .	26
3.6	Plate Properties and Dispersion Curve Analysis . . . . .	27
3.7	Scaling Behavior and Performance Considerations . . . . .	28
<b>4</b>	<b>Results and Discussion</b>	<b>28</b>
4.1	Reference Reconstructions and Defect Definitions . . . . .	28
4.1.1	Discussion . . . . .	31
4.2	Impact of Regularization Parameter on Defect Reconstruction . . . . .	32
4.2.1	Discussion . . . . .	33
4.3	Impact of Noise on Reconstruction . . . . .	34
4.3.1	Discussion . . . . .	36
4.4	Handling Underdetermined Systems with Single Pulse-Echo Reconstruction . . . . .	36
4.4.1	Discussion . . . . .	38
4.5	Sub-Wavelength Resolution . . . . .	39
4.5.1	100 kHz Range . . . . .	39
4.5.2	50 kHz Range . . . . .	41
4.5.3	20 kHz Range . . . . .	42
4.5.4	Discussion . . . . .	43

4.6	Reconstructing Delamination Defects . . . . .	44
4.6.1	Discussion . . . . .	44
4.7	Interpretation and Analysis . . . . .	45
<b>5</b>	<b>Conclusion</b>	<b>45</b>
5.1	Comparison with Industry Standard . . . . .	46
5.2	Comparison with Literature . . . . .	46
5.3	Relation to Signal Theory and Standard Literature . . . . .	47
<b>6</b>	<b>Future Work</b>	<b>47</b>
6.1	Delaminated defect basis . . . . .	47
6.2	Combination of multiple pulse sources . . . . .	48
6.3	Multi-Component Waves . . . . .	48
6.4	Roller-Based Implementation . . . . .	48
6.5	Averaged objects . . . . .	49
6.6	Generalized Tikhonov Regularization . . . . .	49
6.7	Solving for Mounted Parts . . . . .	49
6.8	Virtual Emitters . . . . .	49
6.9	Multi lambda solutions . . . . .	49
6.10	Grid Spacing Optimization . . . . .	50
<b>A</b>	<b>Appendix</b>	<b>50</b>
A.1	Additional Defects . . . . .	50
A.2	Additional Undocumented Tests . . . . .	52
A.3	Introduction to Tikhonov Regularization . . . . .	52
A.4	Tikhonov Regularization and Noise . . . . .	54
A.5	Introduction to Sub-Wavelength Localization . . . . .	54
A.6	LTI systems and impulse responses . . . . .	55
A.7	Sensor Symmetry and Phantom Defects . . . . .	58
A.8	Exploring noise resistance separately . . . . .	59
A.9	Boundary-less results . . . . .	59
A.10	Self-Made Simulation . . . . .	60

# 1 Introduction

## 1.1 Terminology

- LDV: Laser Doppler Vibrometer, a non-contact measurement device that uses laser beams to measure surface vibrations.
- NDT: Non-Destructive Testing, testing of materials or structures without causing damage.
- CFRP: Carbon Fiber Reinforced Polymer, a composite material made of carbon fibers and a polymer matrix, known for its high strength-to-weight ratio.
- Analytical Methods: Techniques which rely on precise mathematical models in continuous domains, such as differential equations.
- Vectorization: A method which fundamentally describes quantities, and even functions in terms of discrete vectors and matrices.
- Digital Twin: A digital representation of a physical object or system, often used for simulation and analysis.
- Transducers: Implicitly shortened form of Piezo-Electric transducers, devices that convert electrical signals into mechanical vibrations and vice versa, used for sending and receiving ultrasonic pulses.
- Calibration: The process of scanning the impulse response over the entire object using an LDV.
- Defect Measurement: Implicitly refers to the response measurement of transducer locations, after the calibration on all locations has been performed.

## 1.2 Ultrasonic NDT: Context and Motivation

Non-destructive testing (NDT) is essential in industries where component failure can have severe or catastrophic consequences, such as aerospace, infrastructure, and high-value machinery. Early detection of faults not only prevents unexpected failures but also extends the operational lifespan of components by reducing unnecessary replacements. The increasing adoption of advanced materials, particularly carbon fiber-reinforced polymers (CFRPs) and other reinforced polymers, introduces challenges for fault detection. These materials are prone to sudden failure without visible faults [1]. Their inhomogeneous and anisotropic properties, along with manufacturing inconsistencies (e.g., variations in polymer type, drilling, fiber orientation, and layering) [2, 3], make accurate simulation and modeling difficult. Furthermore, components are often assembled using adhesives rather than mechanical fasteners, further complicating simulation-based approaches even if perfect composite models were available. Hence, there is a need for NDT methods which are practical and economical for in-service testing of such components [4].

Over the past two decades, advances in personal computing power and the development of highly optimized high-level programming languages have made vectorization of linear problems increasingly practical. Additionally, Laser Doppler Vibrometer (LDV) technology has matured [5], offering high-precision, non-contact measurement of surface vibrations, which allows characterization of complex objects without an underlying theoretical model. The EAPS Wavelab at ETH Zürich is equipped with such an LDV system, and much of the theory and methodology in this thesis is built around the capabilities and data structures provided by this device.

This thesis aims to develop a theoretical foundation for an algorithm which builds a model of the object to be tested almost entirely based on an empirical scan of the object, and making use of this empirical model to enable defect detection by only measuring at a few fixed locations on the object. These fixed locations could be measured using permanently adhered transducers, potentially allowing the testing of components at a press of a button without any setup time and within a few seconds, potentially without any disassembly. While the calibration (scan of the object) and pre-computation of the model can be computationally expensive, the evaluation step is highly efficient both computationally and memory-wise. The aim long term is to develop a system where it is practical to perform a health test of a structure after every usage of the object.

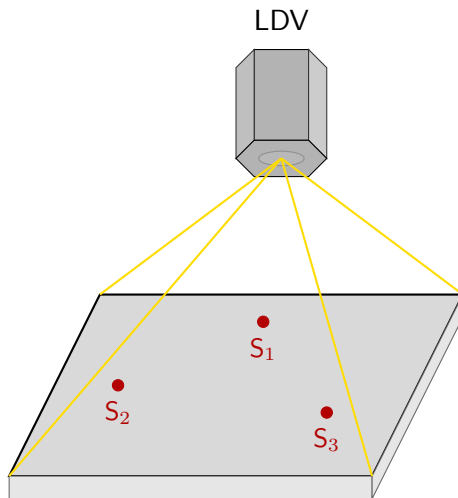


Figure 1: A sketch on a hypothetical setup, where a LDV scans the impulse response over the entire plate for calibration purposes. In this example, three transducers are placed on the object, and emit pulses to which the LDV measures the response. After calibration, the sensors should be able to measure the responses of each other to determine defects.

### 1.3 Summary of Contributions and Key Results

The proposed method was evaluated using the commercial simulation software Salvus from Mondaic [41], with a rectangular aluminum plate serving as the test object. For all intents and purposes, this plate can be regarded to be a dispersive anisotropic medium. It should be noted that the algorithm does not know about the materials shape, nor material properties. The aluminum plate was chosen in parts for comparisons purposes with other methods.

Key findings include:

- The algorithm achieves sub-wavelength localization of simple defects. In simulated aluminum plates, frequencies as low as 20 kHz (minimum wavelengths  $\sim 15$  cm) enable localization down to 2.5 cm, suggesting applicability even with non-ultrasonic transducers.
- It demonstrates strong noise resistance, producing useful results even with 40% RMS noise.
- The method reconstructs the shapes of larger defects (e.g., circles and squares of 5 cm diameter) when using frequencies of at least 50 kHz (minimum wavelengths  $\sim 6$  cm) and can simultaneously detect multiple defects.
- Defect localization is possible with only a single sensor and emitter by leveraging plate asymmetry, but the approach also generalizes to multiple emitters and sensors.

- Delamination-type defects are detectable to some extent. Extending the method to detect delaminations should be straightforward; see Section 6.
- The algorithm does not require precise control over the transducers to emit specific pulses, and can self-correct pulse variations to an extent.

## 1.4 Mathematical Framework (without derivation)

This section provides an overview of the mathematical framework underlying the approach, without detailed derivations. The aim is to give the reader an overview before the full derivation is presented in Section 2, and to help assess the relevance of this thesis to their interests.

### Notation summary:

- Vectors are denoted with arrows, e.g.,  $\vec{m}$ , and always represent time series (discrete, finite length, periodic).
- Matrices are uppercase, e.g.,  $G_{ij}$ , and typically represent convolution operators (Toeplitz/-circulant).
- Subscripts  $i, j, n$  denote spatial locations (transducers or grid points).
- $P$  is a "defect basis" matrix, mapping the abstract defect vector  $\vec{d}$  to the physical space. A proper derivation can be found in section 2

Consider a scenario where a transducer at location  $j$  emits a signal  $\vec{s}_j$ , and another transducer at location  $i$  measures the response  $\vec{m}_i$ . The impulse responses  $G_{in}$  and  $G_{jn}$  describe the propagation from  $i$  or  $j$  to any point  $n$  on the object.

We use a single-scattering system, which in the field of NDT is commonly referred to as the Born approximation [27], meaning every defect and its components only interact with the incident wave once, and then re-emit it. The re-emitted wave does not interact with other defects anymore.

**Remark:** While we use the terminology of the Born approximation as commonly understood in NDT, the mathematical formulation in this work does not strictly apply the Born approximation as defined in [27].

The measured signal at  $i$  is:

$$\vec{m}_i = G_{ij}\vec{s}_j + ([G_{1i}G_{1j}S_j], \dots, [G_{ni}G_{nj}S_j])P\vec{d} \quad (1)$$

Where:

- $\vec{m}_i$ : measured response at  $i$  (vector over time)
- $G_{ij}$ : impulse response matrix between  $i$  and  $j$
- $\vec{s}_j$ : emitted signal from  $j$
- $S_j$ : convolution matrix of  $\vec{s}_j$
- $P$ : defect basis matrix (sparse, block-diagonal, encodes defect type/location)
- $\vec{d}$ : defect amplitude vector (each entry corresponds to a defect at a grid location)

We can recast the problem as:

$$\begin{aligned}\vec{\mathbf{m}}_{ij} &= \mathcal{L}_{ij}\vec{d}, \quad \text{where} \\ \vec{\mathbf{m}}_{ij} &:= \vec{m}_i - G_{ij}\vec{s}_j \\ \mathcal{L}_{ij} &:= ([G_{1i}G_{1j}S_j], \dots, [G_{ni}G_{nj}S_j])P\end{aligned}\tag{2}$$

For multiple emitter/receiver pairs, we "stack" the system [26]:

$$\begin{pmatrix} \vec{\mathbf{m}}_{12} \\ \vec{\mathbf{m}}_{13} \\ \vdots \end{pmatrix} = \begin{pmatrix} \mathcal{L}_{12} \\ \mathcal{L}_{13} \\ \vdots \end{pmatrix} \vec{d} := \vec{\mathbf{m}}_{full} = \mathcal{L}_{full}\vec{d}\tag{3}$$

Increasing the amount of information in the system reduces ambiguity in the solution for  $\vec{d}$ .

At this stage, the problem becomes a basic linear algebra task. In general, for real-world problems, such a matrix has no unique solution, or no solution at all. Tikhonov regularization is employed, minimizing  $\|\mathcal{L}_{full}\vec{d} - \vec{\mathbf{m}}_{full}\|^2 + \lambda\|\vec{d}\|^2$  for some empirically chosen  $\lambda$  [6, 8, 34].

The Tikhonov inverse of an arbitrary matrix  $M$  is defined as:

$$M^{\text{Tik}} := (M^T M + \lambda I)^{-1} M^T\tag{4}$$

where  $I$  is the identity matrix.

The defect vector is then obtained by:

$$\vec{d} = \mathcal{L}_{full}^{\text{Tik}} \vec{\mathbf{m}}_{full}\tag{5}$$

This formulation frames the inverse problem as a regularized linear system, enabling non-iterative computation of defect profiles from measured data. While the inversion can be computationally intensive, evaluating equation 5 is highly efficient. Such efficiency is especially valuable in cases where real-time evaluation of a pre-determined problem is desired. As a result, the main computational effort is concentrated in the initial calibration phase, which only needs to be performed once.

**Remark: On the Source Term and linear quantities** In this thesis, the source term  $\vec{s}_j$  at each transducer is defined as the measured signal at the transducer location, including all initial and reflected waves. This empirical approach avoids the need to model or separate direct and reflected components, simplifying calibration and ensuring mathematical consistency. See Section 2.4 for details.

## 1.5 The Thesis in Context

This section places the mathematical framework of the thesis in the context of existing approaches, highlighting key methodological trends and their relevance to the present work. Rather than providing a comprehensive literature review, the focus is on summarizing the main classes of methods and clarifying how this thesis relates to them, with references to relevant literature where appropriate.

### 1.5.1 Vectorization and Linear Algebraic Approach

A key feature of this method is its reliance on vectors and matrices, rather than on continuous functions or differential equations. This vectorized approach [30], as seen in the Foldy method [9], is particularly well-suited to empirical data acquisition, such as LDV measurements, which naturally yield time series data. By representing all quantities as vectors, the method avoids imposing restrictive assumptions that would otherwise be necessary to translate measurements into a purely functional or analytical form.

This formalism enables the use of linear algebra techniques, most notably Tikhonov regularization [6, 8, 34], which is central to the results in this thesis. While alternative regularization strategies exist [34], the Tikhonov inverse (equation 4) is foundational here. This stands in contrast to the Wiener filter [12], a popular noise reduction method in signal processing, which requires assumptions about the noise and signal characteristics, which are not made in this thesis.

The importance of the Tikhonov inverse in this thesis cannot be overstated, as it plays many roles: it is used for noise reduction in impulse response calculation, regularization of unstable inverse problems, noise reduction in defect localization, and provides suitable boundary conditions to solve highly underdetermined systems. Almost every aspect in this thesis uses the Tikhonov regularization in some form.

### 1.5.2 Empirical and Analytical Models

Another distinguishing aspect of this thesis is its minimal reliance on analytical models. The method is built directly on measured impulse responses, making only a few general assumptions about how quantities are connected. This empirical approach is similar to that in [19], where measurements are used to characterize the object with few assumptions, or [20] where delamination in steel reinforced concrete is detected by estimating the thickness of the object by comparing the resonant echo frequencies of an excitation.

In contrast, analytical methods can use a range of analytical models [11, 7] to describe wave propagation. [22, 18, 24] are examples of methods based on analytical models. While these models are powerful for well-characterized, predictable media (e.g., air in radar applications [33]), they are less flexible for NDT of composites or reinforced concrete, where manufacturing inconsistencies can lead to significant variations between specimens. The increasing maturity of LDV technology enables a more empirical, object-specific approach.

### 1.5.3 Relation to Digital Twins and Waveform Inversion

Waveform inversion [15, 16, 17] represents a hybrid between empirical and analytical model based approaches. These methods use measured wave data to iteratively adjust a forward model until simulated and measured responses match, explicitly including defects in the model. Alternatively, a digital twin of the undamaged structure can be constructed as a reference for future defect detection. The approach in this thesis shares similarities with digital twin methods, as it uses a calibration of the healthy object to empirically determine the system response.

At the Center of Immersive Wave Experimentation at ETHZ, collaboration with Mondaic [41] has led to a wave inversion method for composite materials [32], using LDV measurements to create digital twins and simulate wave propagation. This work inspired the present thesis. My own experience manufacturing composite parts for an ARIS-Rocketry-Team highlighted practical concerns in composite modeling, such as hand-manufactured inconsistencies, woven

carbon fiber fabrics, and glued components among many others. These factors are difficult to capture in digital models. A key outcome of the Mondaic project was the development of a defect detection algorithm that, leveraging a digital twin, could identify defects with far fewer LDV measurements than required for the initial inversion. This thesis addresses that outlook by proposing such a method.

#### 1.5.4 Industry Standard: Echo-Based and C-Scan Methods

Any new NDT method must be evaluated in the context of established industry practices, as relevance is defined by comparison with these standards rather than solely with academic literature. The following summary is based on discussions with professionals in the aircraft industry.

The prevailing industry standard for ultrasonic NDT, especially in composite materials, is based on echo techniques. In these methods, a pulse is emitted into the material and the reflected signals are analyzed. The most common implementation is the C-scan, where a pulse-echo transducer is mechanically scanned across the surface, emitting ultrasonic pulses and recording echoes at each position. This produces a visual map of internal features such as delaminations or voids.

These techniques primarily use time-of-flight (TOF) measurements: the travel time of a reflected pulse is used to estimate the location of a defect.

A strength of the C-scan approach is due to it being highly empirical and not depending on precise analytical models, making it highly flexible. The upfront cost is relatively low, relying mainly on a handheld device and associated software [28, 38, 39].

C-scan systems typically require mechanical scanning devices, often roller-based transducers that must physically roll over the entire surface. This limits their practicality for large, highly curved or hard to access structures.

### 1.6 Thesis objective

This thesis introduces an algorithm that enables defect evaluation of an object after a single comprehensive calibration scan. Future inspections require measurements at only a few fixed points, which may be obtained using permanently installed transducers for fully remote and automated monitoring.

The method is first derived, then evaluated on simulated data. Its performance is characterized by varying defect types, noise levels, system parameters, and wavelengths, allowing strengths and limitations of the approach to be assessed.

## 2 Mathematical derivation

### 2.1 Modeling Assumptions

We assume the following properties from the object in question:

1. The object is linear
2. The object is invariant over time
3. The object is reciprocal, meaning the impulse response between any two points is equal in both directions.

4. A defect interacts with an incoming wave by nearly immediately re-emitting it.
5. Enforced condition: Time is periodic. This is technically not an assumption as any time invariant object can be imposed to be periodic. The following section describes this in more detail.

From now on, the linear quantity will be named "signal", "wave" or "pulse".

**Note:** The description of what kind of waves exactly we are measuring (Lamb waves, for example) has been excluded on purpose. The model does not make any assumptions about the nature of the waves that propagate within the material and what is measured. In principle, we could easily extend this methodology to electromagnetic waves by making few changes to account for wave directionality. In our case, the quantity we are measuring is the out-of-plane velocity of the propagating guided wave over the flat object.

## 2.2 On periodic time

The initial field is assumed to be zero. For testing, pulses are emitted from transducer locations on the object, and the responses measured at other locations. Everything that is measured is the result of the pulses that were emitted, with noise being an exception, which is handled later on.

If the emitted signals are repeated periodically, all responses everywhere are also periodic. Therefore, we can mathematically treat the time of the object to be periodic too.

This approach aligns naturally with the operation of many Laser Doppler Vibrometers (LDVs), which often function in a periodic regime by sending out pulses at regular intervals and recording the system's response for some periods. This periodic excitation and measurement scheme allows for efficient averaging and noise reduction, and fits seamlessly into the mathematical framework adopted here.

The resulting advantage being, that we do not need to arbitrarily truncate the time, leading to loss in data, and it properly justifies the use of the Fourier series transform, as we will see in the next subsection 2.3.

**Remark:** In linear time-invariant (LTI) systems, the Fourier basis functions are eigenfunctions of any system operator. This means that each frequency component evolves independently, and only frequencies present in the measured data can influence the system's response. A discrete time measuring device naturally only has access to a limited amount of frequencies. All other frequencies cannot affect the measured data, it is safe to ignore them. The discrete treatment of time is therefore not an approximation.

## 2.3 Behavior of a Linear quantity inside a time invariant object

In order to obtain information to work with, we may start by choosing two different points  $i, j$  on the material. We emit a source signal on  $i$ , and measuring its response in  $j$ . Due to linearity, we can describe the impulse response using a linear transformation  $G$ :

$$G\vec{v}_i = \vec{w}_j \tag{6}$$

where  $\vec{v}_i$  denotes a source term at location  $i$ , and  $\vec{w}_j$  the response at location  $j$ .

In real-world applications, the measurements have discrete time steps and have finite length, hence the vectors are finite dimensional. Due to time invariance, such a transformation takes

the shape of a Toeplitz matrix [29]. The Periodic time domain moreover changes the form of the matrix to be of circular Toeplitz shape:

$$G = \begin{pmatrix} g_0 & g_n & \cdots & g_1 \\ g_1 & g_0 & \cdots & g_2 \\ \vdots & \vdots & \ddots & \vdots \\ g_n & g_{n-1} & \cdots & g_0 \end{pmatrix} = \vec{g}^* \quad (7)$$

This matrix may be interpreted as a circular convolution using a vector  $\vec{g} := (g_0, g_1, \dots, g_n)$ , or in other terms,  $G\vec{v} = \vec{g} * \vec{v}$ . All circular Toeplitz matrices are Diagonalized under the Discrete Fourier Transform Basis, being highly important for numerical efficiency [35] as we can perform convolutions in the frequency domain by simple component wise multiplication. It ends up reducing certain parts of this thesis computation time from hours down to seconds.

These Matrices, or functions will be called "Impulse Response functions". Capital and lower case of the same letters implicitly correspond to the same matrix, but in Matrix of Vector form as in 7. From now, impulse responses between two points are labeled as  $G_{ij}$  to denote the locations of the source and receiver locations. Note that  $G_{ij} = G_{ji}$  due to the reciprocity assumption from section 2.1.

How the components of  $\vec{g}$  are determined can be found in section 2.9.

## 2.4 The generalized linear quantity

In the previous section, we established the impulse response between two "linear quantities." Here, we clarify what this means and highlight the flexibility this generalized approach provides compared to standard wave propagation descriptions.

Recall that this thesis relies on LDV measurements of a "linear quantity". Specifically for this case, the out-of-plane velocity of the object. Suppose we scan the impulse response of the object at the location of an emitter. The measurement at the source location is denoted as  $\vec{s}_i$ .

The measured signal  $\vec{s}_i$  at the source location is not a pure excitation term; rather, it represents the total response at that point, including the initial pulse and all subsequent reflections and re-reflections. The LDV records this composite signal at a single point, which is a superposition of waves traveling in various directions, information that cannot be separated by the LDV. Section 3.3 provides a visualization of this concept using the data from this thesis.

This ambiguity in what the LDV actually measures is a challenge for traditional physical models, which typically require a clear distinction between the excitation and the system's responses. In contrast, the approach in this thesis focuses on relating "what is measured at one location" to "what is measured at another," without needing to isolate the initial excitation. A partial mathematical justification for this approach is provided in section A.6, where it acts as a foundation on how to abstract this thesis further to various other problem statements.

## 2.5 Behavior of Defects

Consider a wave propagating through the medium and encountering a defect. By the assumptions of linearity and time invariance 2.1, the defect's effect can be modeled as a linear, time-invariant operation at its location. Specifically, the incoming wave  $\vec{v}$  at a defect is re-emitted

as a new source  $\vec{w}$  at the same location:

$$\vec{w} = D\vec{v} = \begin{pmatrix} d_0 & d_n & \cdots & d_1 \\ d_1 & d_0 & \cdots & d_2 \\ \vdots & \vdots & \ddots & \vdots \\ d_n & d_{n-1} & \cdots & d_0 \end{pmatrix} \vec{v} = \vec{d} * \vec{v} \quad (8)$$

Here,  $\vec{d}$  represents the defect's reflection properties.

The central objective of this algorithm is to solve for the defect vectors at every location. To reduce the number of unknowns, we make a simplifying assumption: each defect vector  $\vec{d}$  is modeled as a unit (delta) vector, representing an instantaneous response at a specific location.

In line with the fourth modeling assumption 2.1, this means  $\vec{d}$  is typically taken as a discrete delta pulse. i.e., a vector with  $d_0 = a$  (amplitude) and all other entries zero. Thus, each defect is characterized solely by its amplitude at its location. More general cases, where the models deviate from this model are discussed in section 2.7.

## 2.6 System Matrix Assembly

The goal is to construct a linear operator (matrix)  $\mathcal{L}$  such that  $\vec{m} = \mathcal{L}\vec{d}$ , where:

- $\vec{m}$ : measured wave responses at specific locations on the object.
- $\vec{d}$ : abstract defect vector encoding defect amplitudes at grid points.

**Notation reminder:**

- $G_{ij}$ : impulse response matrix (convolution operator) between  $j$  to  $i$ . Equivalent to  $\vec{g}_{ij}^*$  as defined in equation 7.

The wave propagation is described in terms of reflection orders, counting how many times waves reflect off defects. For a source pulse at location  $i$  ( $\vec{s}_i$ ) and a measured response at  $j$  ( $\vec{m}_j$ ):

**0th order (no defects):**  $\vec{m}_j = G_{ij}\vec{s}_i$ .

**1st order (Born approximation):** The source signal reflects off each defect once. A wave starting at  $i$ , propagating to a point  $k$ , re-emitting at  $k$ , and propagating to  $j$  is expressed as  $\vec{g}_{kj} * \vec{d}_k * \vec{g}_{ik} * \vec{s}_i$ . See Figure 2 for a visualization.

**Note:** The boundaries of the object are treated as part of the medium itself, so are not affected by reduction to the first order approximation.

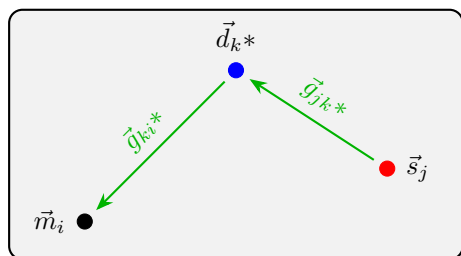


Figure 2: Visualization on how a source at location  $j$  propagates to a defect at location  $k$ , which then re-emits the wave. Afterwards, it propagates to a receiver location  $i$ . As an equation, the image visualizes  $\vec{m}_i = \vec{g}_{kj} * \vec{d}_k * \vec{g}_{ik} * \vec{s}_j$ .

Summing over all grid points  $k$  gives:

$$\vec{m}_i = \vec{g}_{ij} * \vec{s}_j + \sum_k \vec{g}_{kj} * \vec{d}_k * \vec{g}_{ik} * \vec{s}_j = G_{ij} \vec{s}_j + ([G_{1i} D_1 G_{1j}], \dots, [G_{ni} D_n G_{nj}]) \vec{s}_j \quad (9)$$

- **Notation clarification:**

- All variables in uppercase denote matrices.
- $\vec{m}_i$  is a vector.
- $G_{ij} \vec{s}_j$  represents a matrix-vector multiplication.
- Horizontal stacking of matrices is written as  $([A_1], \dots, [A_n])$ , where each block (e.g.,  $[G_{1i} D_1 G_{1j}]$ ) is a product of matrices.
- The vector  $\vec{s}_j$  is converted to a matrix  $S_j$  via the convolution operation, as described in equation 7.

The RHS expression of equation 9 is the matrix formulation of the problem.

We can leverage the symmetry of the convolution operation:  $\vec{a} * \vec{b} = \vec{b} * \vec{a}$  to re-order equation 9 as:

$$\vec{m}_i = \vec{g}_{ij} * \vec{s}_j + \sum_k \vec{g}_{kj} * \vec{g}_{ik} * \vec{s}_i * \vec{d}_k = G_{ij} \vec{s}_j + ([G_{1i} G_{1j} S_j \vec{d}_1], \dots, [G_{ni} G_{nj} S_j \vec{d}_n]) \quad (10)$$

Where the source pulse  $\vec{s}_i$  is now treated as a predefined constant.

The first vector expression is just a reordering of 9. The RHS Matrix is the analogous formulation in matrix form. Unlike the matrix formulation in equation 9, where the structure is naturally of form  $m = \mathcal{L}\vec{s}$ , 10 does not naturally have such a property for the defect vectors  $\vec{d}_i$ .

We reform the matrix expression as follows:

$$\vec{m}_i - G_{ij} \vec{s}_j = ([G_{1i} G_{1j} S_i], \dots, [G_{ni} G_{nj} S_i]) \begin{pmatrix} \vec{d}_1 \\ \vdots \\ \vec{d}_n \end{pmatrix} \quad (11)$$

Since the dimensionality of  $\vec{m}_i$  and  $\vec{d}_n$  are equal for all n, the problem is vastly under determined. We make use of assumption 4 of section 2.1.

For simplicities sake, hinting at section 2.5, we first assume each defect  $\vec{d}_i$  has form of a unit vector for index 0:  $\vec{d}_i = (d_i, 0, 0, \dots)$ . Due to this each defect at every location only has one degree of freedom ( $d_i$ ). We define the macroscopic defect vector  $\vec{\mathbf{d}} = (d_0, d_1, \dots, d_n)$ . This macroscopic defect vector defines all defects on the object through its coefficients.

In order to find an expression using this in equation 10, we define the defect projector operator  $P$  defined as:

$$\begin{pmatrix} \vec{d}_1 \\ \vec{d}_2 \\ \vdots \\ \vec{d}_n \end{pmatrix} = P \vec{\mathbf{d}} \quad (12)$$

Such a defect projector in the current simplified assumptions look like:

$$P = \begin{pmatrix} \vec{e}_0 & & \\ & \ddots & \\ & & \vec{e}_0 \end{pmatrix}, \quad \vec{e}_0 := \begin{pmatrix} 1 \\ 0 \\ \vdots \\ 0 \end{pmatrix} \quad (13)$$

Thus, the problem can be rewritten as:

$$\vec{m}_i - G_{ij}\vec{s}_j = ([G_{1i}G_{1j}S_i], \dots, [G_{ni}G_{nj}S_i])P\vec{d} = ([G_{1i}G_{1j}S_i\vec{e}_0], \dots, [G_{ni}G_{nj}S_i\vec{e}_0])\vec{d} \quad (14)$$

Note that the RHS expression is mentioned because this is the efficient way to implement this numerically. The expression  $([G_{1i}G_{1j}S_i], \dots, [G_{ni}G_{nj}S_i])$  is very memory inefficient to load, even using sparse matrices in Fourier domain. Hence in practice, each block  $[G_{1i}G_{1j}S_i\vec{e}_0]$  is computed separately before putting together into the full expression.

We can redefine the components in the following manner to obtain the desired structure  $\vec{m} = \mathcal{L}\vec{d}$ :

$$\begin{aligned} \vec{m}_{ij} &= \mathcal{L}_{ij}\vec{d}, \quad \text{where} \\ \vec{m}_{ij} &:= \vec{m}_i - G_{ij}\vec{s}_j \\ \mathcal{L}_{ij} &:= ([G_{1i}G_{1j}S_j], \dots, [G_{ni}G_{nj}S_j])P \end{aligned} \quad (15)$$

This system, if solved for  $\vec{d}$ , finds the defect for a system, where one emitter at location  $j$  sends out a pulse, and a sensor at  $i$  measures it. This can work decently well in certain conditions and is documented in section 4.4.

In practice, it is highly beneficial to have multiple emitters and/or sensors to obtain more information to solve the system. This can be extended easily by simply stacking the system:

$$\begin{pmatrix} \vec{m}_{21} \\ \vec{m}_{31} \\ \vdots \end{pmatrix} = \begin{pmatrix} \mathcal{L}_{21} \\ \mathcal{L}_{31} \\ \vdots \end{pmatrix} \vec{d} \quad := \quad \vec{m}_{full} = \mathcal{L}_{full}\vec{d} \quad (16)$$

In this case, the first row described the pulse measurement at location 2, sent from 1 (or equivalently vice versa), and the second row a pulse from location 1 to 3. This would be equivalent to a system in which one emitter, and two sensors are present.

## 2.7 Generalizing the Defect Space

We generalize the defect space to allow for more complex defect behaviors. This section is not strictly necessary to understand the results of this thesis.

In the previous section, for simplicities sake, the assumption was made that all defects act like perfect reflectors:  $\vec{d}_i \propto \vec{e}_0$  where  $\vec{e}_0$  as in the previous section is the unit vector for index 0.

This essentially means that any incoming wave is convolved with a delta function, essentially re-emitting the wave nearly instantaneously.

We denote this as the basis of the defect space. Recalling equation 13, we can extend the defect projector Matrix in the general form:

$$P = \begin{pmatrix} (P_{sub-1}) & & & \\ & (P_{sub-2}) & & \\ & & \ddots & \\ & & & (P_{sub-n})) \end{pmatrix} \quad (17)$$

Where the Matrix is now composed of submatrices  $(P_{sub-i})^c$ . In equation 13, every sub-matrix had the form of a vector  $\vec{e}_0$ . In general, we can assign any arbitrary basis for every sub-matrix:

$$P_{sub-i} = \begin{pmatrix} \vec{b}_1^i & \vec{b}_2^i & \dots \end{pmatrix} \quad (18)$$

Where  $\vec{b}_n^i$  denotes the n-th defect basis vector for location  $i$ .

The corresponding form of the macroscopic defect vector is:

$$\vec{\mathbf{d}} = \begin{pmatrix} \vec{d}^1 \\ \vdots \\ \vec{d}^n \end{pmatrix}, \quad \vec{d}^i = \begin{pmatrix} d_1^i \\ d_2^i \\ \vdots \end{pmatrix} \quad (19)$$

Instead of every defect location having one index defining it as in the previous section, now each has a vector with multiple indexes.

Examples for a practical basis are:

$$P_{sub-i} = (\vec{e}_0 \quad \vec{e}_1 \quad \vec{e}_{-1}) = \begin{pmatrix} 1 & 0 & 0 \\ 0 & 1 & 0 \\ \vdots & \vdots & \vdots \\ 0 & 0 & 1 \end{pmatrix} \quad (20)$$

A basis which allows the defect to delay the re-emitted pulse by one time step.

$$P_{sub-i} = (\vec{e}_0 \quad \vec{e}_1 \quad \vec{e}_{-1}) \quad (21)$$

Or alternatively, one which has proven itself to be remarkably useful, a basis of band limited  $\vec{e}_0$  pulses.

$$P_{sub-i} = (\vec{e}'_0 \quad \vec{e}''_0) \quad (22)$$

Where  $\vec{e}'_0$  and  $\vec{e}''_0$  are band limited pulses, obtained by setting the frequency components of the  $\vec{e}_0$  vector to 0 at certain intervals. For example, the lowest and highest halves of the frequency spectrum.

Looking back at equation 14, with the new generalized defect projector, the system matrix  $\mathcal{L}_{full}$  becomes:

$$\vec{m}_i - G_{ij} \vec{s}_j = ([G_{1i}G_{1j}S_j], \dots, [G_{ni}G_{nj}S_j]) P \vec{\mathbf{d}} = ([G_{1i}G_{1j}S_j P_{sub-1}], \dots, [G_{ni}G_{nj}S_j P_{sub-n}]) \vec{\mathbf{d}} \quad (23)$$

For the most part, the most simple basis from equation 13 suffice in the experiments made for this Thesis.

The effects of the defect bases presented here are briefly discussed in Appendix A.2

## 2.8 Impulse Response Construction using Tikhonov Regularization

This section describes how the impulse response was calculated. While the method used is likely not novel, it appears that the approach is rather uncommon in this field, hence it has been documented and derived here. It is not essential to the core algorithm, but seems to be a good way of implementing noise reduction properties into the impulse response function itself, without making any assumptions about the noise characteristics, as in the widely used Wiener filter method [12]. One may skip this section, by just assuming we know the impulse

responses on the object. Especially considering how this section can be substituted by various other methods.

We consider the problem of estimating the impulse response  $g_{in}$  between a source location  $i$  and a measurement location  $n$  using repeated measurements. Let:

- $\vec{r}_p^i$ : the  $p$ -th measured source pulse at location  $i$  (reference signal, time domain, vector length  $T$ )
- $\vec{r}_p^n$ : the  $p$ -th measured response at location  $n$  (time domain, vector length  $T$ )
- $p = 1, \dots, P$ : index over repeated measurements (periods)
- $*$ : denotes circular convolution

The convolutional model is:

$$\vec{r}_p^i * \vec{g}_{in} = \vec{r}_p^n \quad (24)$$

Switching to the frequency domain (denoted by  $\hat{\cdot}$ ), convolution becomes point-wise multiplication [35]:

$$\hat{r}_p^i(f) \cdot \hat{g}_{in}(f) = \hat{r}_p^n(f) \quad (25)$$

where  $f$  indexes the discrete Fourier frequencies, meaning we consider each frequency component  $f$  separately.

**Note:** The exact definition of the Fourier transform is not critical here, as long as it diagonalizes the circular convolution and remains consistent throughout all computations, which can be achieved using various conventions. In this thesis, the Real Discrete Fourier Transform (RDFT) is used, implemented in the Julia programming language via the `rfft` function from the FFTW package [40]. The RDFT reduces memory usage by storing only the positive frequency components, as the negative frequencies are the complex conjugates of the positive ones. As a sidenote, the source cited does not actually show the analytical expression for the RFFT, as this library is very poorly documented, so the following expression has been derived by guessing, and validating in code.

For a real-valued input vector  $\vec{r} = (r_1, \dots, r_N)$  of length  $N$ , the Fourier transform is defined as

$$\hat{r}(f) = \sum_{n=1}^N r_n e^{-2\pi i (fn)/N}, \quad f = 0, 1, \dots, \lfloor \frac{N}{2} \rfloor.$$

This corresponds to the non-redundant positive frequency components up to the Nyquist frequency. In Julia, these are returned in array indices  $1, 2, \dots, \lfloor N/2 \rfloor + 1$ , with  $f = 0$  stored in the first entry.

Here,  $r_n$  is the  $n$ -th time step (1-based indexing as in Julia),  $N$  is the total number of samples, and  $f$  indexes the discrete frequency bins.

Stacking all  $P$  measurements for a fixed frequency  $f$ , we have:

$$\begin{pmatrix} \hat{r}_1^i(f) \\ \vdots \\ \hat{r}_P^i(f) \end{pmatrix} \hat{g}_{in}(f) = \begin{pmatrix} \hat{r}_1^n(f) \\ \vdots \\ \hat{r}_P^n(f) \end{pmatrix} \quad (26)$$

This is a linear system for the scalar  $\hat{g}_{in}(f)$  at each frequency  $f$ .

Tikhonov regularization is a well known method for solving ill-posed inverse problems [6]. A short derivation and explanation can be found in Appendix A.3.

The Tikhonov regularized solution for  $\hat{g}_{in}(f)$  is given by minimizing the following cost function:

$$\hat{g}_{in}^{\text{reg}}(f) = \arg \min_g \|\vec{r}^i(f)g - \vec{r}^n(f)\|^2 + L|g|^2 \quad (27)$$

where  $\vec{r}^i(f)$  and  $\vec{r}^n(f)$  are  $P$ -dimensional vectors of the  $p$ -th measurement at frequency  $f$ , and  $L$  is the regularization parameter.

The minimization problem is quadratic in  $g$  and can be solved analytically. Taking the derivative with respect to  $g^*$  and setting it to zero yields [14]:

$$\frac{\partial}{\partial g^*} (\|\vec{r}^i(f)g - \vec{r}^n(f)\|^2 + L|g|^2) = 0 \quad (28)$$

which leads directly to the closed-form solution:

$$\hat{g}_{in}^{\text{reg}}(f) = \frac{\sum_{p=1}^P \hat{r}_p^i(f)^* \hat{r}_p^n(f)}{\sum_{p=1}^P |\hat{r}_p^i(f)|^2 + L} \quad (29)$$

where  $*$  denotes complex conjugation.

### Summary of notation:

- $i$ : source (reference) location
- $n$ : measurement location
- $p$ : measurement repetition index
- $f$ : frequency index (after DFT)
- $\hat{r}_p^i(f)$ : DFT of the  $p$ -th reference signal at  $i$ , frequency  $f$
- $\hat{r}_p^n(f)$ : DFT of the  $p$ -th response at  $n$ , frequency  $f$
- $L$ : regularization parameter (real, positive)

In practice, the regularization parameter  $L$  should be set to a small positive value. Setting  $L$  to zero can result in singularities, while excessively large values may lead to unpredictable behavior. The results are generally insensitive to the precise value of  $L$  as long as it remains small.

**Remark:** The regularization parameter  $L$  in this section is not to be confused with the regularization parameter  $\lambda$  in the Tikhonov solution of section 2.9. They both perform the same function, but for different problems. In all other sections of this thesis, when the Regularization parameter is mentioned, it refers to  $\lambda$  of other sections.

**Remark:** In standard theory, the above solution is optimal for complex-valued data. However, in early implementation for this thesis, it was observed that treating  $g$  as a real number (initially as a mistake) produced more meaningful impulse responses. Using the proper complex solution led to noisy results occasionally. Therefore, for all results shown, the real-valued version was used:

$$\hat{g}_{in}^{\text{reg}}(f) = \frac{\sum_{p=1}^P \hat{r}_p^i(f) \hat{r}_p^n(f)}{\sum_{p=1}^P \hat{r}_p^i(f)^2 + L} \quad (30)$$

The poor performance of the complex result likely may be due to numerical instability. I did not find a reason why the real-valued version would yield proper results. These finding were based on a self written simulation in earlier stages of this thesis. Later comparisons with new (Salvus) data revealed both equations yielded the same results. I did not investigate further.

## 2.9 Regularized Inverse Problem and Tikhonov Solution

Once the system matrix  $\mathcal{L}_{full}$  and the measurement vector  $\vec{\mathbf{m}}_{full}$  are assembled, the inverse problem is to recover the defect vector  $\vec{d}$  from the linear system:

$$\vec{\mathbf{m}}_{full} = \mathcal{L}_{full}\vec{d} \quad (31)$$

In practice, this system is often ill-posed or under determined due to noise, incomplete data, or limited measurement configurations. To obtain a stable and physically meaningful solution, Tikhonov regularization is applied [8, 36, 6].

The regularized solution is defined as the minimizer of the following cost function:

$$\vec{d}_{reg} = \arg \min_{\vec{d}} \left\{ \|\mathcal{L}_{full}\vec{d} - \vec{\mathbf{m}}_{full}\|^2 + \lambda \|\vec{d}\|^2 \right\} \quad (32)$$

where  $\lambda > 0$  is the regularization parameter, controlling the trade-off between data fidelity and solution smoothness.

The Tikhonov inverse of a matrix  $M$  is defined as:

$$M^{\text{Tik}} := (M^T M + \lambda I)^{-1} M^T \quad (33)$$

where  $I$  is the identity matrix of appropriate size. Applying this to our system yields the closed-form solution:

$$\vec{d}_{reg} = \mathcal{L}_{full}^{\text{Tik}} \vec{\mathbf{m}}_{full} \quad (34)$$

Once  $\mathcal{L}_{full}^{\text{Tik}}$  is computed, it can be saved and used for any measurements very quickly using a matrix-vector multiplication. Hence, the evaluation of a measurement can be done by even comparatively weak computers.

The optimal value of  $\lambda$  can vary depending on the specific defect scenario and data characteristics. In this thesis, it was found most effective to test a range of  $\lambda$  values spanning several orders of magnitude (e.g., 1, 10, 100, 1000), as different cases may require different levels of regularization for best results.

## 2.10 Modified Regularization Matrix for Transducer Self-Correction

In practice, the regularization matrix  $I$  in the Tikhonov term can be replaced by a diagonal matrix  $R$  where the entries corresponding to transducer locations are set to zero, i.e.,

$$R_{kk} = \begin{cases} 0 & \text{if } k \text{ corresponds to a transducer location} \\ 1 & \text{otherwise} \end{cases} \quad (35)$$

This modification allows the algorithm to automatically correct for amplitude variations or inconsistencies at the transducer sites, by placing virtual "defects" directly at the sensors to change its properties without being restricted by regularization. All other locations are regularized as before. This approach was found to enhance the stability and accuracy of defect reconstructions in the presence of fluctuating test pulse amplitudes.

Using more general defects, as discussed in section 2.7 allows the algorithm to potentially even account for small delays in the test pulse automatically.

The defects at the transducer locations themselves are to be removed from the final data. Using a single emitter system likely improves the ability of the system to self-correct.

## 2.11 Explicit System Configurations

The general inverse problem is formulated as:

$$\vec{\mathbf{m}}_{full} = \mathcal{L}_{full}\vec{d} \quad (36)$$

where:

- $\vec{\mathbf{m}}_{full}$ : stacked measurement vector (all sensor/emitter pairs)
- $\mathcal{L}_{full}$ : assembled system matrix (linear operator)
- $\vec{d}$ : defect amplitude vector (unknowns to solve for)

The matrix  $\mathcal{L}_{full}$  is constructed by stacking individual operator blocks  $\mathcal{L}_{ij}$  and the corresponding measurement vectors  $\vec{\mathbf{m}}_{ij}$  for each sensor-emitter pair  $(i, j)$ :

$$\mathcal{L}_{full} = \begin{pmatrix} \mathcal{L}_{12} \\ \mathcal{L}_{13} \\ \vdots \\ \mathcal{L}_{1n} \end{pmatrix} \quad \vec{\mathbf{m}}_{full} = \begin{pmatrix} \vec{\mathbf{m}}_{12} \\ \vec{\mathbf{m}}_{13} \\ \vdots \\ \vec{\mathbf{m}}_{1n} \end{pmatrix} \quad (37)$$

Each block  $\mathcal{L}_{ij}$  has the structure:

$$\mathcal{L}_{ij} = ([G_{1i}G_{1j}S_j], \dots, [G_{ni}G_{nj}S_j])P \quad (38)$$

where  $G_{ki}$  and  $G_{kj}$  are impulse response matrices,  $S_j$  is the source convolution matrix, and  $P$  is the defect basis/projector.

**Configurations:**

- **Pulse-Echo (Single Sensor):**

$$\mathcal{L}_{full} = \mathcal{L}_{11} \quad (39)$$

- **Single Emitter with  $n$  sensors:**

$$\mathcal{L}_{full} = \begin{pmatrix} \mathcal{L}_{12} \\ \mathcal{L}_{13} \\ \vdots \\ \mathcal{L}_{1n} \end{pmatrix} \quad (40)$$

for  $n$  sensors measuring the response from a single emitter at location 1.

- **Five Sensor/Emitter (Alternating):**

$$\mathcal{L}_{full} = \begin{pmatrix} \mathcal{L}_{21} \\ \mathcal{L}_{31} \\ \mathcal{L}_{41} \\ \mathcal{L}_{51} \\ \mathcal{L}_{12} \\ \mathcal{L}_{32} \\ \mathcal{L}_{42} \\ \mathcal{L}_{52} \\ \vdots \end{pmatrix} \quad (41)$$

For example, with 3 sensors (1,2,3), the full matrix is:

$$\mathcal{L}_{full} = \begin{pmatrix} \mathcal{L}_{21} \\ \mathcal{L}_{31} \\ \mathcal{L}_{23} \end{pmatrix}$$

This configuration obtains the most information for a system where the transducers can switch between emitter and receiver modes, and measure the responses themselves.

In principle the configuration can be chosen arbitrarily, and is mostly restricted in how the measurements are obtained in practice.

## 2.12 Algorithm Summary

The algorithm proceeds as follows:

1. Perform a one-time calibration scan of the object, measuring wave propagation from each transducer location.
2. Construct impulse responses between all relevant points using the Born approximation (see Section 2.8).
3. Treat the source term as fixed, and reformulate the problem as a linear system with the defect vector as the unknown (see Section 2.6).
4. Assemble the full system matrix by stacking individual system matrices according to the chosen measurement configuration (see Section 2.11).
5. Solve the system using Tikhonov regularization to address underdetermined or ill-posed cases (see Section 2.9).
6. Once the Tikhonov-inverted matrix is computed, defect evaluation from new measurements can be performed rapidly via matrix-vector multiplication.

## 3 Methodology

All references to computation speed in this thesis refer to a Lenovo Thinkpad T16 with an Intel Gen13 i7 CPU with multithreading. The following sections outline the general structure of the code, simulation methodology, and provide example plots to visualize the internal data structure, clarifying the algorithm's operation.

### 3.1 General Structure and Data Handling

Due to the large size of the data, which would exceed memory constraints if loaded all at once, the code uses a pseudo-class structure, mimicking a class structure by saving and loading data in a folder structure. Functions such as `func(object_name::String, ...)` act like methods, and project-specific variables are managed internally via a dedicated file (accessed with `get_variable(object_name::String)`), remaining hidden from the user.

All data is bandpass filtered to the desired frequency range during object initialization and stored in the real-Fourier domain as HDF5 files. User-facing functions are defined in `command_center.jl`. Below is a pseudocode example of typical usage:

```
# Create a new object, set up its folder, and store
# associated metadata
```

```

initialize_new_object(object_name, data_frequency, other vars...)

# do for all raw data
add_raw_data(object_name, active_sensor, other vars...)

# do for all defect measurements
add_measurement(object_name, sensor, defect_name, other vars...)

# calculate impulse response once all raw data has been added
calculate_greens_function(object_name, lambda)

# different methods available for different matrix structures
# creates and saves the system matrix
create_reduced_system_matrix(object_name, lambdas, other vars...)

# evaluates a defined defect using the system matrix
evaluate_matrix(object_name, defect_name, other vars...)

# other plotting functions available

```

Wave data is stored as a 2D array with shape  $(n, t)$ , where  $n$  indexes spatial locations and  $t$  indexes time steps. The algorithm processes data in a 1D format without explicit spatial awareness during calculations. Spatial mapping is handled via a xyz file that assigns 3D coordinates to each array index, used only for visualization. This structure assures flexibility for arbitrary geometries and matches the native format of our laboratory's LDV system.

Sensors are referenced by integer indices mapped to corresponding coordinates. When adding data, the active transducer index and measurement location are specified. Multiple measurements are automatically grouped for noise handling.

All data is Fourier transformed and bandpass filtered before saving in HDF5 format using real-valued FFT (RFFT). A typical raw dataset in our simulations (10,000 time steps at 100kHz, 10,201 spatial locations) requires approximately 400MB per transducer in Float32 format.

### 3.2 Simulation, Raw Data, and Visualization

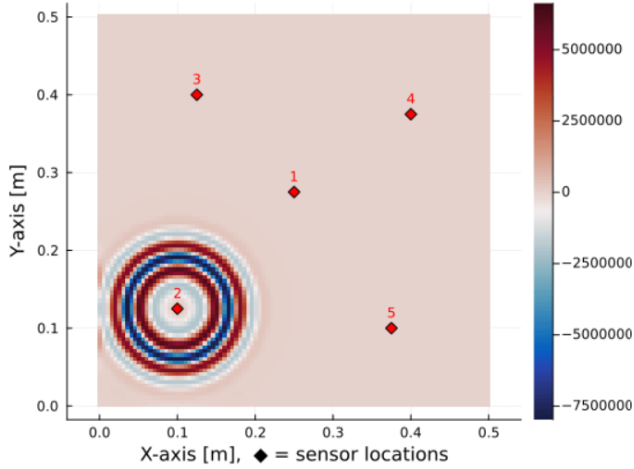
Simulations were performed using Salvus from Mondaic [41] on a  $50\text{ cm} \times 50\text{ cm} \times 9\text{ mm}$  aluminum plate. Most tests used five transducers emitting a 50kHz Ricker wavelet. Simulations ran for 10ms.

The simulated plate is homogeneous and isotropic, with transducers placed at the corners and center as described in Section 4.1. The initial excitation is a Ricker wavelet at 50 kHz central frequency, and data is bandpass filtered to the desired frequency range. Salvus [41] is used with plate parameters  $v_p = 6142.03\text{ m/s}$ ,  $v_s = 3093.85\text{ m/s}$ , and  $\rho = 2710\text{ kg/m}^3$ . Attenuation is modeled using a quality factor  $Q = 250$ , ensuring wave energy dissipates within 10 ms. The resulting data is treated as periodic, with the period optionally shortened by summing over integer fractions (e.g., 5 ms, 3.33 ms) the code used to run the simulations can be found in [37]. The code cannot be run without a Salvus license.

Impulse response functions were obtained by simulating wave propagation over the defect-free plate once for each transducer, with responses saved on a  $101 \times 101$  grid. This one-time calibration step is the most data-intensive part of the process.

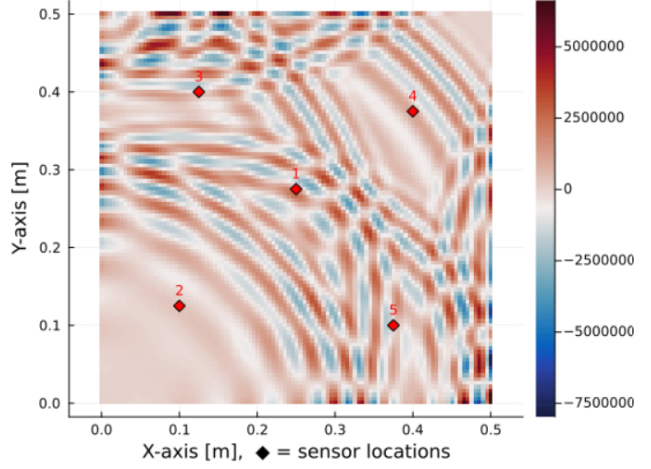
For defect simulations, data was saved only at the transducer locations.

Raw data with emitter 2 at time 0.06 ms



(a) Salvus Wave simulation at 0.06ms

Raw data with emitter 2 at time 0.19 ms

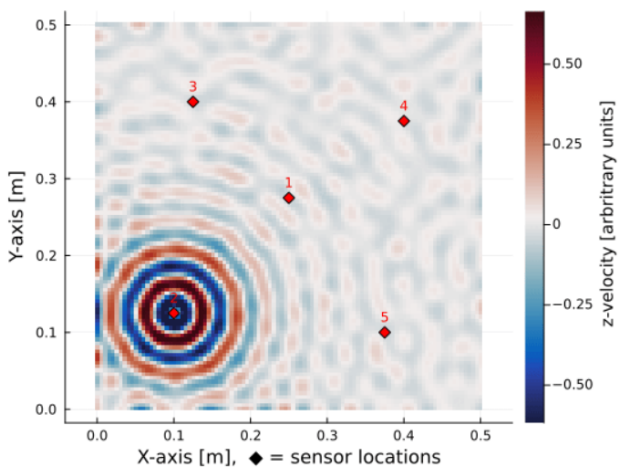


(b) Salvus Wave simulation at 0.19ms

Figure 3: Wave simulation at two different times. The emitter locations are labeled from 1 to 5. The colorbar indicates the z-axis velocity. Note: the scale is distorted due to suboptimal simulation settings.

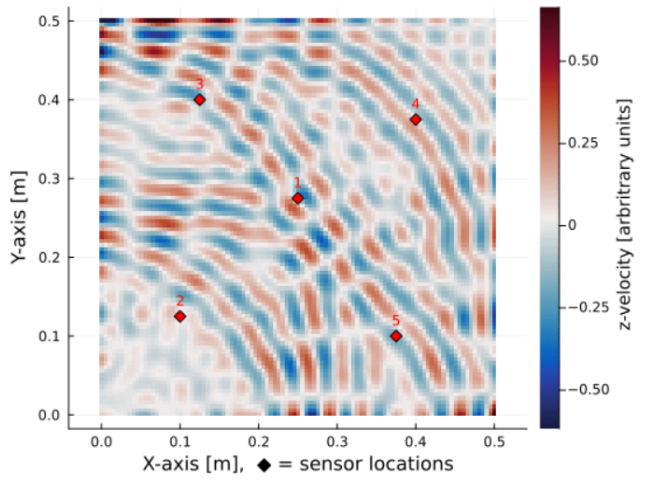
Figures 3 represent the raw data directly from the simulation. Unlike the actual simulation, only points on a 101x101 grid were saved. If we wish to properly test in the periodic time domain, we may subdivide the time domain into smaller chunks, and add the data together. The data is bandpass filtered to a desired frequency range. An example being shortening to a period length of 5ms, and lowpass filtering to 50khz, where the data transforms as Figure 4.

Raw data with emitter 2 at time 0.06 ms



(a) Salvus Wave simulation at 0.06ms

Raw data with emitter 2 at time 0.19 ms



(b) Salvus Wave simulation at 0.19ms

Figure 4: Wave simulation at two different times, lowpass filtered to 50khz. The emitter locations are labeled along their numbering from 1 to 5. The z-velocity has been normalized.

Figure 4 represents the data as it is used by the algorithm, and is internally saved as this.

We note that the short pulse shape of the original wave as in Figure 3 has been compromised due to low pass filtering, and that waves from the previous period are still present when the new period starts as seen in Figure 4a. Due to the time periodic nature of the algorithm, this is not a problem.

Normalization of the z-velocity is required because the raw values are on the order of  $10^6$ , which causes numerical instabilities due to precision loss (Larger step sizes between numbers). As long as normalization is applied consistently to all measurements, the simulation results remain unaffected.

In this thesis, one of the simulations was analyzed to find the maximum absolute value of the z-velocity across all time and space, which was then used as the normalization factor for all data.

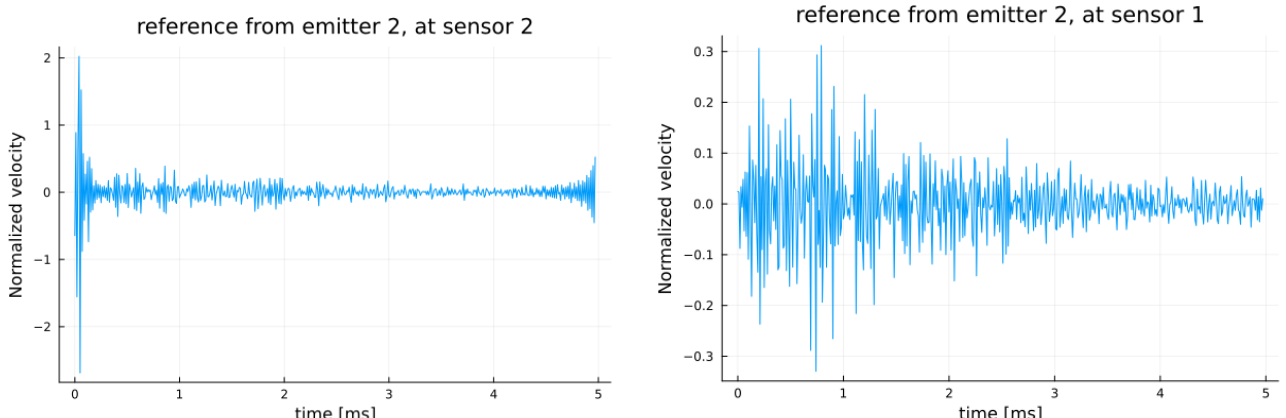
Sensor numbering is arbitrary and assigned during object initialization. Each pixel in the 101x101 grid of Figure 4 corresponds to a unique internal location; for example, the sensors 1 to 5 are indexed as [5016, 2046, 2606, 8156, 7596], and all other points from 1 to 10201 represent plate locations. The ordering is managed externally and does not influence the algorithm or results, nor does the algorithm have knowledge of the spatial relationships between points.

All data, including these measurements, are Fourier transformed before being saved.

### 3.3 Impulse Response Calculation and Visualization

The mathematical details for impulse response calculation are provided in Section 2.8. The implementation is located in `Modules/greens_block_finder_V2.jl` [37]. The process is highly efficient: handling 10 GB of input data and producing 2 GB of impulse response data takes about 10 seconds. Further speedup via multithreading is minimal, indicating that disk I/O is the main bottleneck and the computation itself is already near optimal.

In the algorithm, the source is derived directly from the raw data of Figure 4 by measuring the corresponding location. For example:

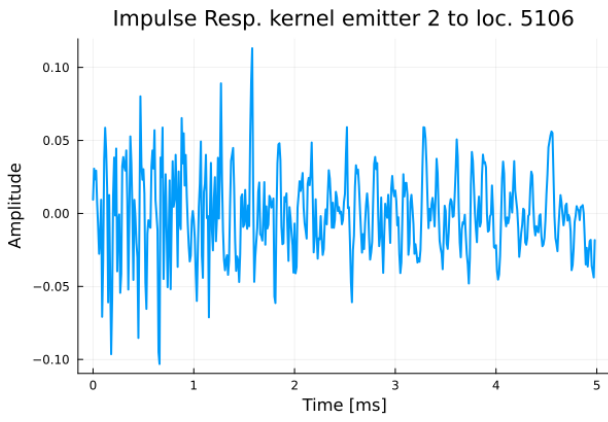


(a) Measured source pulse from Figure 4. Note how the reflections are considered part of the source.

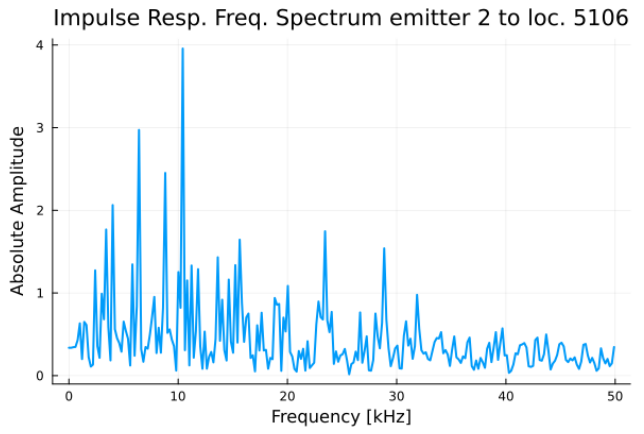
(b) Response at the location of sensor 1.

Figure 5: The source sent out at sensor 2, and the resulting response at sensor 1.

The resulting impulse response function is visualized as follows:



(a) Impulse response function between sensor 2 and sensor 1 in time domain. "Location 5106" refers to the location where sensor 1 is located in the internal 1D coordinate system.



(b) Impulse response function between sensor 2 and sensor 1 in frequency domain.

Figure 6: The kernel which connects the source and response between sensor 2 and sensor 1 of Figures of 4 via convolution.

In practice, multiple noisy measurements are available (usually 5 in this thesis), where the best fitting impulse response function (in the code called Green's function) is calculated using the method described in section 2.9. Note that this is done from all sensors, to all locations on the plate.

Furthermore, note how the notion of causality does not exist here. There is no "before and after" as a concept in periodic time. This would be even more clear if we were to plot the time axis as going from -2.5ms to 2.5ms instead of 0 to 5ms (circular shift).

### 3.4 System Matrix Assembly and Inversion

Section 2.6 notes that practical adjustments are needed to implement the system matrix for equations 15 and 23:

$$\mathcal{L}_{ij} = ([G_{1i}G_{1j}S_j], \dots, [G_{ni}G_{nj}S_j])P = ([G_{1i}G_{1j}S_j P_{sub-1}], \dots, [G_{ni}G_{nj}S_j P_{sub-n}]) \quad (42)$$

To avoid inefficient matrix multiplications, each component  $[G_{ni}G_{nj}S_j P_{sub-n}]$  is computed separately, using the Fourier basis for efficient element-wise multiplication for each row of the  $P_{sub-n}$  matrix:

```
for i in 1:defect_dimensionality
    submatrix_block[:, i] = G1[n, :] .* G2[n, :] .* P_sub[:, i]
end
# .* in this language is component-wise multiplication
```

$G1$  corresponds to  $\vec{g}_{ni}$ , and  $G2$  to  $\vec{g}_{nj} * \vec{s}_j$ .  $P_{sub} = P_{sub-n}$  for all  $n$ , as all locations have the same defect basis in this thesis.

Using sparse matrices for this step resulted in longer computation times, likely due to frequent redefinitions and writes, though this may be implementation-dependent.

See `Modules/MatrixGenerator.jl` [37] for details.

Building the full system matrix for multiple sensors is simply a matter of stacking the  $\mathcal{L}_{ij}$  matrices, as described in Section 2.11.

The inversion of the system matrix is the most computationally intensive step in the workflow. The process uses Tikhonov regularization (see section 2.9), implemented as follows (pseudo-code):

```
M_tik = (M*M' + lambda*I) \ (M)',
```

Here,  $M$  is the system matrix,  $M'$  its adjoint,  $\text{lambda}$  the regularization parameter, and  $I$  the identity (or generalized regularization) matrix. The Julia backslash operator efficiently solves the linear system without explicitly computing the inverse (as would be the case with `inv(M*M' + lambda*I)*M'` just like in equation 4), which improves numerical stability and memory usage.

A note on notation: equation 4 uses transposes rather than adjoints. This was an oversight on my part, discovered late in the process. However, in practice, using the transpose instead of the adjoint did not noticeably affect the results.

The actual implementation supports generalized regularization matrices, but the core logic remains as shown above. For details, see `Modules/MatrixGenerator.jl` [37].

For the largest matrix size used in this thesis ( $10,201 \times 10,000$ ), the inversion step takes about one minute on an Intel Gen13 i7 CPU. While this is acceptable for moderate problem sizes, both computation time and memory usage scale poorly with increasing defect space (roughly  $N^2$ ). With 16GB RAM (about 9GB available for computation), the practical limit for matrix size is around  $10,000 \times 30,000$ , corresponding to about 1.2GB for Float32 storage. This is lower than expected given available memory, likely due to implementation inefficiencies.

In summary, while the inversion step is feasible for the system sizes presented here, scaling to larger problems will require further optimization or alternative numerical approaches.

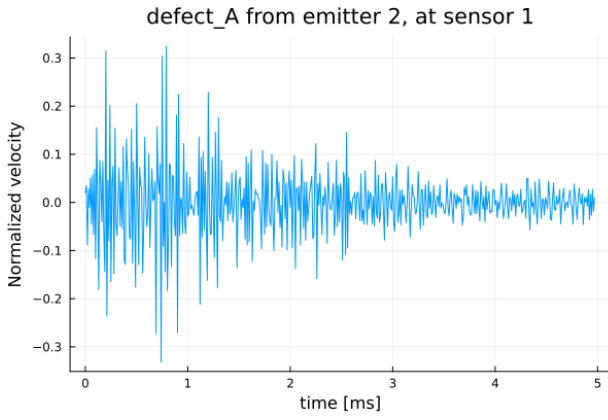
### 3.5 Defect Evaluation and Visualization

Once the inverted system matrices (one for each  $\lambda$  value) have been computed and saved, defect evaluation becomes straightforward.

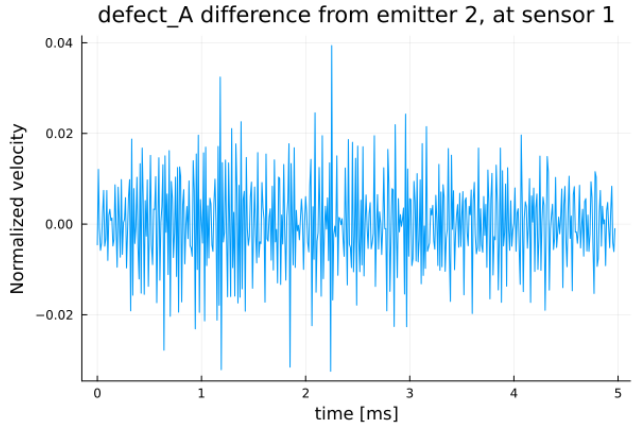
Referring to equations 15 16, the required measurement vector  $\vec{m}_{full}$  consists of measurements at the transducer locations  $i$  with an active source at  $j$ , taken while the object contains the defect to be investigated. The term  $G_{ij}\vec{s}_j$  is the raw impulse response from the calibration data.

Applying the matrix-vector multiplication in equation 34 is highly efficient, typically taking less than a second including data loading. This step scales linearly with matrix size and can be performed in sections, so it does not require loading the entire matrix into memory. As a result, defect evaluation is practical on almost any modern computer, supporting the goal of enabling rapid field usage.

To evaluate the defect using the system matrix, the reference responses (defect-less responses) between sensors are stored and subtracted from the corresponding measurements taken with the defect present.



(a) The defect measurement at sensor 1 with emitter at sensor 2. This is the same measurement as in Figure 5b, but with a defect present.



(b) The difference between the defect measurement and the reference measurement at sensor 1. Or in other words Figure 5b subtracted by Figure 7a.

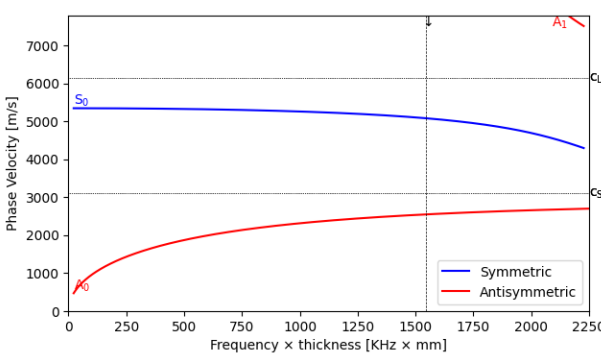
Figure 7: Measurement of a defect and the difference to the reference measurement which is fed into the system matrix for evaluation. Note the scale difference between the two plots.

Figure 7b is what is fed into the system matrix for evaluation (in frequency domain). It is the change in signal caused by the defect present. The actual nature of the defect is documented in Figure 9, being circular with 1.5cm diameter.

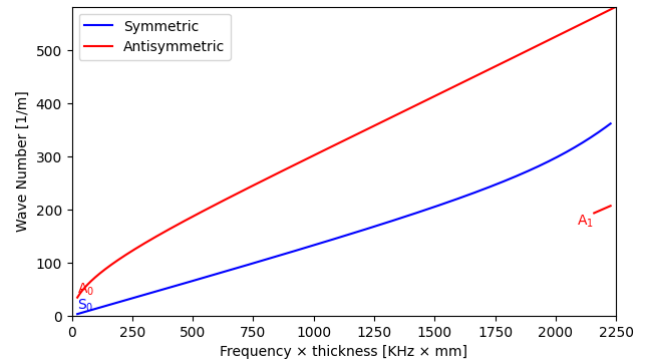
The construction of a system matrix is described in section 2.6. The final measurement of Figure 7b is treated as a vector  $\vec{m}_{12}$ , which depending on the system matrix is combined with different measurement vectors by appending all together, as described in section 2.11. Afterwards, it is just a matrix-vector multiplication.

### 3.6 Plate Properties and Dispersion Curve Analysis

For analysis of spatial resolution and wave propagation, the wavelengths of guided waves in the plate are determined from analytical dispersion curves. These are computed using the Python package [42]:



(a) Phase velocity of the plate.



(b) Wave number of the plate.

Figure 8: Analytical dispersion curves of Lamb waves in an aluminum plate. Parameters: thickness = 9 mm,  $v_p = 6142.03 \text{ m/s}$ ,  $v_s = 3093.85 \text{ m/s}$ , consistent with Salvus simulations. Code available in the GitHub repository [37].

For discussions on wavelengths and resolutions, the main interest is the minimum wavelength for a given frequency range. From Figure 8b, the wave number increases steadily with frequency, so the shortest wavelength is determined by the highest frequency in the band. Therefore, the minimum wave velocities can be read off by reading the phase velocities off 8a, and computing through  $\lambda = \frac{v_p}{f}$ .

The relevant minimum wavelengths for this thesis are

$f_{\max}$	$\lambda_{\min}$	(43)
100 kHz	2.2 cm	
50 kHz	3.5 cm	
20 kHz	6.2 cm	

where  $f_{\max}$  is the highest frequency in the band.

### 3.7 Scaling Behavior and Performance Considerations

A matrix  $M$  of size  $n \times m$  stored in Float32 format requires  $4 \cdot n \cdot m$  bytes of memory. During matrix inversion, an additional  $n \times n$  matrix is created, consuming  $4 \cdot n^2$  bytes, plus some overhead for temporary variables. On a laptop with 16GB RAM (about 9GB available for computation), practical testing showed that the maximum manageable matrix size is approximately  $10,000 \times 30,000$ , or about 1.2GB for Float32 storage. This is less than the theoretical limit, likely due to implementation overhead.

Computationally, matrix inversion scales as  $O(m^2n)$ , where  $m$  is the number of defect parameters and  $n$  is the number of measurements. Increasing the number of measurements is relatively inexpensive, while increasing the number of defect parameters is computationally costly. This is an important consideration when applying the method to larger objects. The inversion process (backslash operator) being purely linearly algebraic, it can natively be implemented for GPU use in the Julia programming language.

Recall that this process is only required to be done once, after which defect evaluation is very fast.

## 4 Results and Discussion

Given the exploratory nature of this thesis, I first present a reference reconstruction to demonstrate the algorithm's performance under ideal conditions. Subsequently, a series of results are shown, each exploring the impacts of individual changes in isolation.

### 4.1 Reference Reconstructions and Defect Definitions

The following results use the alternating 5-sensor system configuration as described in Section 2.11. Five transducers are placed on the object, each sending out a test pulse while the other four measure the response. Since the impulse response between two points is symmetric, measuring both directions is redundant. The system matrix  $\mathcal{L}_{full}$  is assembled according to the stacking scheme outlined in equation 41.

Given that the object has  $101 \times 101 = 10,201$  grid points, and the input data is effectively measured at 10 locations, the resulting inverted system matrix has a size of  $10,201 \times 10,000$ , making it just barely underdetermined. The inversion of this matrix takes roughly a minute on a standard laptop (13th Gen Intel Core i7), and the evaluation of each measurement takes less than a second.

Additional defect simulations not listed here can be found in Appendix A.1. All defect densities in this chapter are modeled as 0.2 times the surrounding aluminum density, with a slight tapering applied to each defect.

Note that colorbars are always plotted relative to the maximum value in each plot. To compare amplitudes, refer to the maximum value indicated on the colorbar.

The simulated object is a  $50\text{ cm} \times 50\text{ cm} \times 9\text{ mm}$  aluminum plate, with transducers placed at the corners and the center of the plate (shown as red dots in the figures).

A 50 kHz central frequency Ricker wavelet is used for excitation, and the data is downsampled to include only frequencies up to 100 kHz.

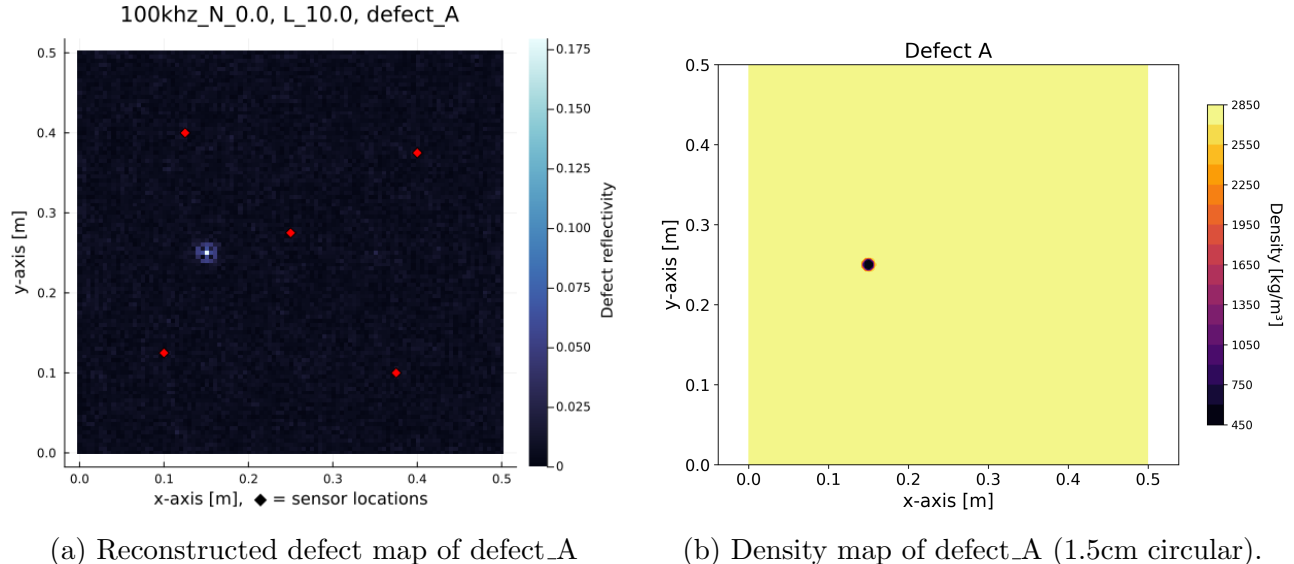
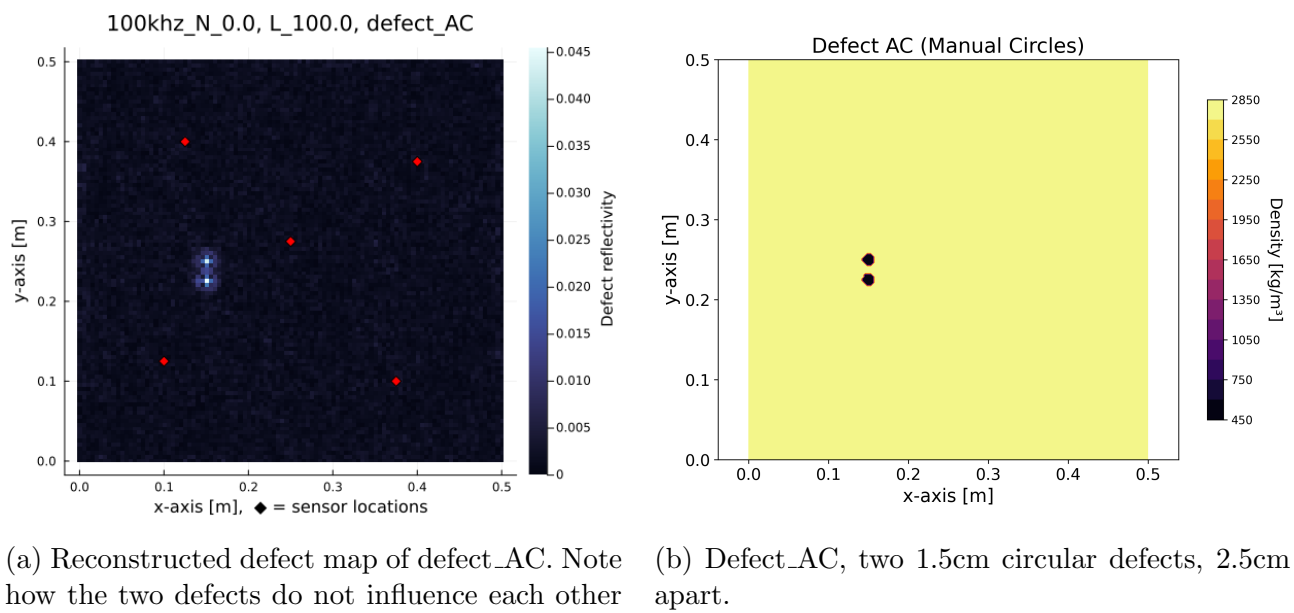


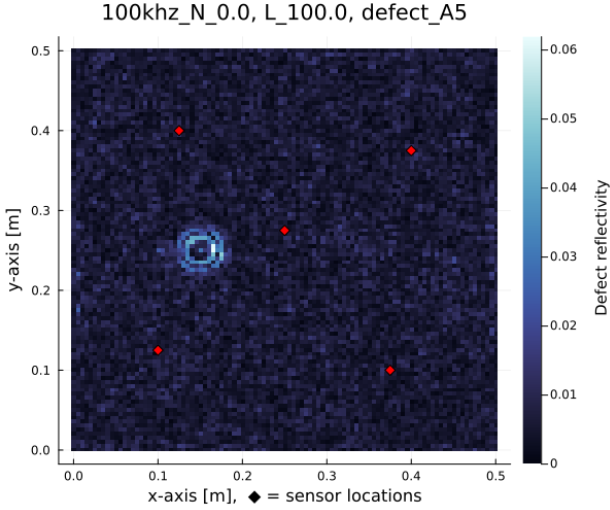
Figure 9: Defect\_A reconstruction with  $\lambda = 10.0$ , 5 sensor-emitter configuration. The reconstruction appears mostly point-like, with a slight halo around it.



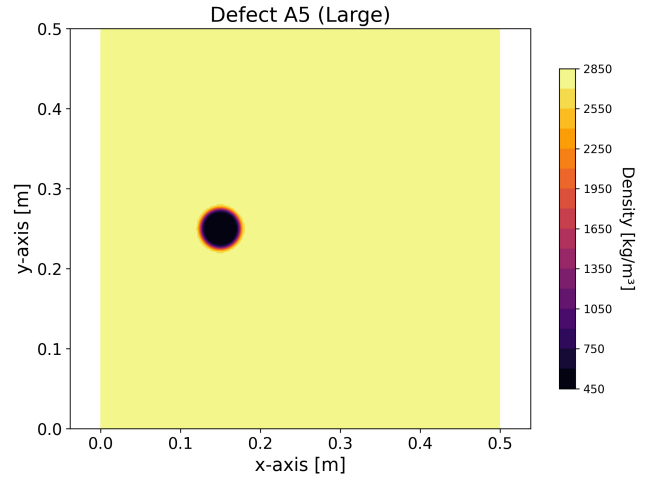
(a) Reconstructed defect map of defect\_AC. Note how the two defects do not influence each other much.

(b) Defect\_AC, two 1.5cm circular defects, 2.5cm apart.

Figure 10: Defect\_AC reconstruction with  $\lambda = 100.0$ , 5 sensor-emitter configuration.

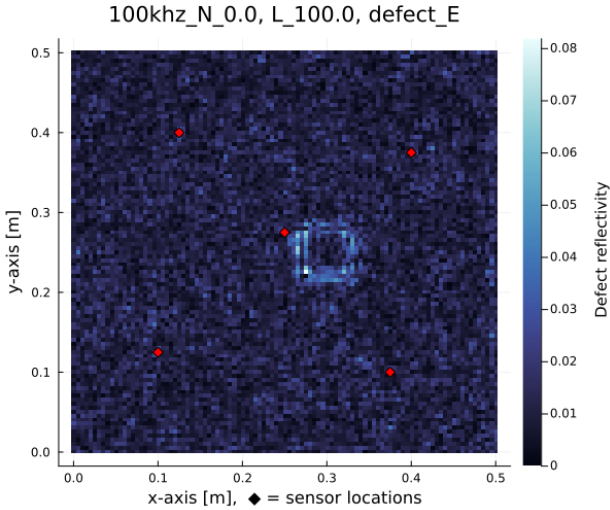


(a) Reconstructed defect map of defect\_A5

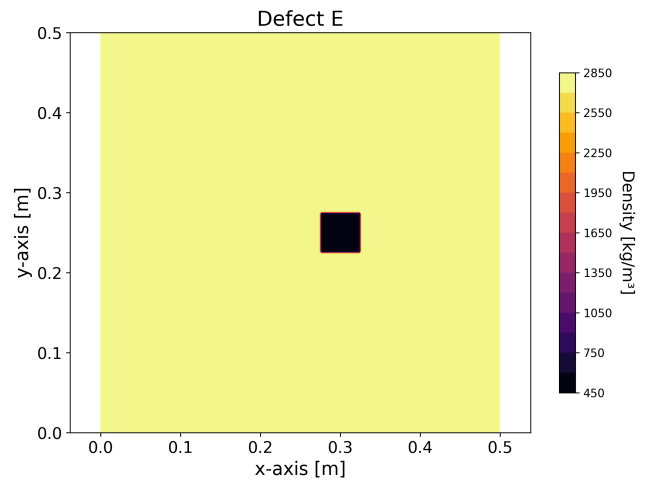


(b) A 5cm diameter circular defect at the same location as defect\_A.

Figure 11: Defect\_A5 reconstruction with  $\lambda = 100.0$ , 5 sensor-emitter configuration. The reconstruction appears as a ring. The background noise artifacts are more strongly pronounced compared to previous figures. We notice that the edges facing the middle of the plate are more pronounced. This defect tests the ability to reconstruct shapes and larger defects.

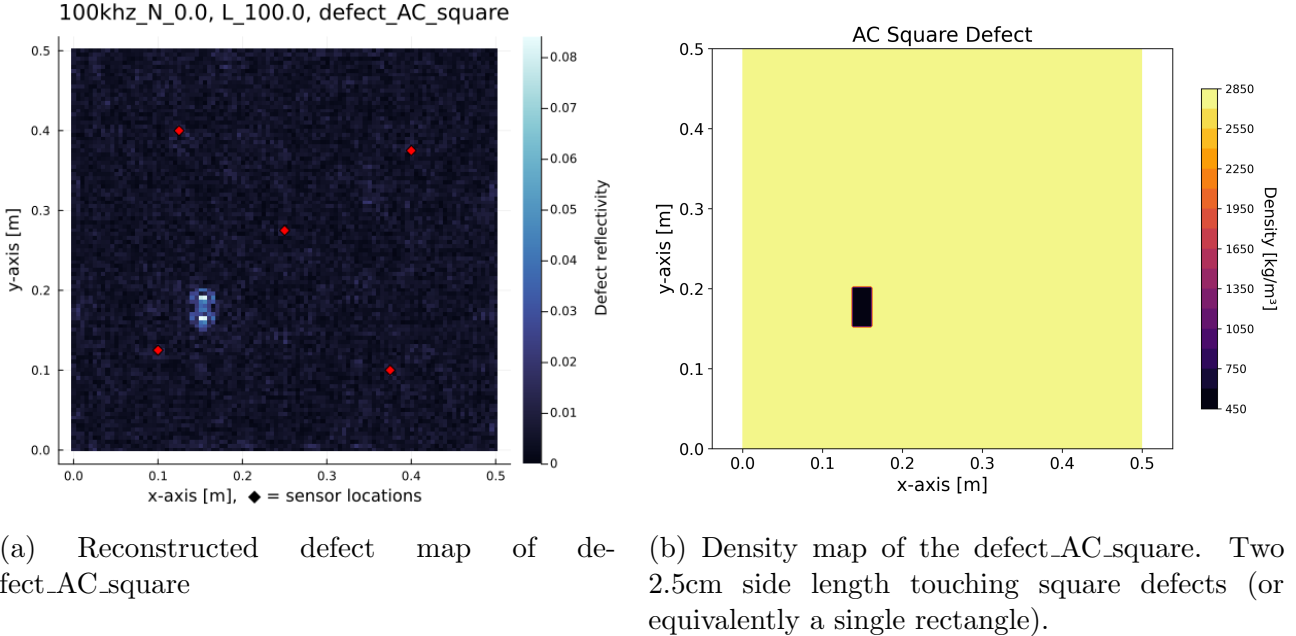


(a) Reconstructed defect map of defect\_E



(b) Density map of the defect E. A 5cm side length square defect.

Figure 12: Defect\_E reconstruction with  $\lambda = 100.0$ , 5 sensor-emitter configuration. The background noise artifacts become more pronounced than in defect\_A5 despite similar sizes. The reconstruction also displays the edges of the shape, but is noticeably less clean. We notice that the edges facing the middle of the plate are again more pronounced. This defect tests the ability to reconstruct a different shape than a circular one.



(a) Reconstructed defect map of defect\_AC\_square

(b) Density map of the defect\_AC\_square. Two 2.5cm side length touching square defects (or equivalently a single rectangle).

Figure 13: AC-square reconstructions with  $\lambda = 100.0$ , 5 sensor-emitter configuration. The defect, which can be considered to be a rectangle has been reconstructed as two point-like defects, similar to defect\_AC (Fig10).

#### 4.1.1 Discussion

These results demonstrate the algorithm's capabilities under favorable conditions: no noise and a frequency range yielding a minimum wavelength of  $\lambda_{min} \approx 2.2$  cm (see equation 43 with  $f_{max} = 100$  kHz).

Defects A and AC (Figures 9 and 10) highlight the algorithm's ability to reconstruct small defects. Notably, in the case of Defect AC, even though the defects are closely spaced, secondary reflection effects do not significantly impact the reconstruction of either defect. The defects exhibit a point-like structure with a slight halo around them. This behavior likely arises because the defect size of 1.5 cm is comparable to the wavelength of 2.2 cm, placing the defect in a regime where it is neither fully sub-wavelength (acting purely point-like) nor large enough to exhibit strong shape effects. This interpretation becomes clearer when considering larger defects and lower frequencies in later sections.

Defects A5 and E (Figures 11 and 12) evaluate the algorithm's ability to reconstruct larger shapes. Both defects are approximately 5 cm in size, slightly exceeding the minimum wavelength of 2.2 cm. The reconstructions primarily highlight the edges of the defects, with the interiors appearing mostly hollow. This is expected, as the algorithm identifies regions where waves scatter, which typically occurs at boundaries where the refractive index changes. A notable observation is that defect reconstructions tend to appear stronger towards the center of the plate. This is likely a consequence of the Born approximation: waves generally approach defects from the plate's center. As a wave enters the defect, part of its energy reflects off the boundary. When the wave exits the defect, another reflection occurs, but with reduced energy due to prior losses. The Born approximation does not account for this energy reduction, leading to an overemphasis on the defect's reflectivity facing the most probable direction of wave incidence. Defect E, being square-shaped, appears less stable in the reconstruction compared to the circular Defect A5. This instability is likely due to the algorithm attempting to reconstruct higher-order effects that are incompatible with the Born approximation. The appearance of

a dot in the center of the A5 defect may indicate such effects. Circular defects align better with the wavefronts, making them more stable in the reconstruction. This hypothesis could be tested by simulating a highly anisotropic medium, where wavefront shapes differ, potentially favoring non-circular defect stability.

Defect AC\_square (Figure 13) is particularly interesting. It consists of two touching square defects, effectively forming a rectangle. The reconstruction, however, shows two distinct point-like defects rather than a continuous shape. This supports the idea, observed in Defect A, that when the wavelength is larger than the defect, the defect appears more point-like, and surface features cannot be resolved. Although the height of the rectangle exceeds the wavelength and should theoretically be resolvable, the algorithm instead separates the defect into two distinct point-like features.

As a whole, we observe the algorithm working with defects around the wavelength size, with smaller defects appearing point-like and larger defects emphasizing edges.

## 4.2 Impact of Regularization Parameter on Defect Reconstruction

The regularization parameter  $\lambda$  plays a critical role in balancing noise suppression and defect amplitude accuracy. The following Figures illustrate its effects using Defect\_A and Defect\_E as examples. For the defect definitions, see Figures 9 and 12. The results are shown for  $\lambda = 10.0$ , 100.0, and 1000.0 with no noise, using the 5 sensor-emitter configuration.

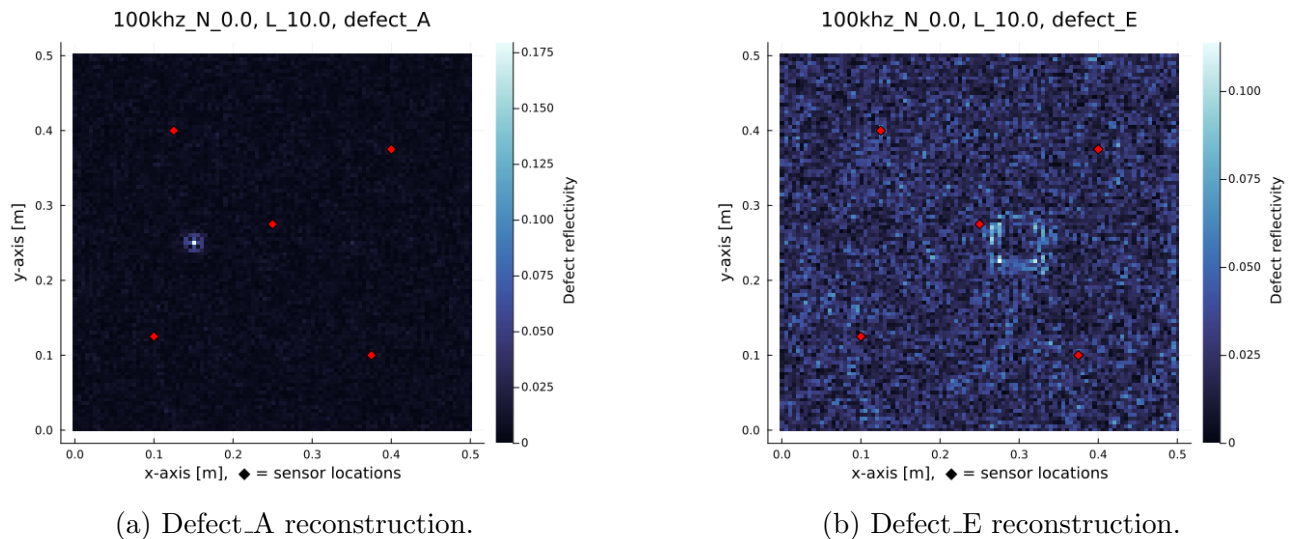
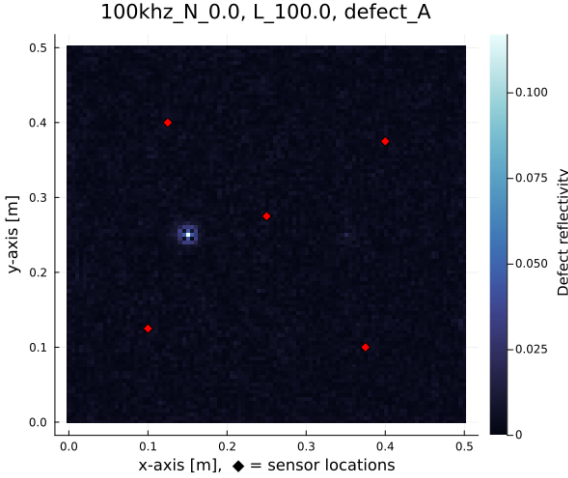
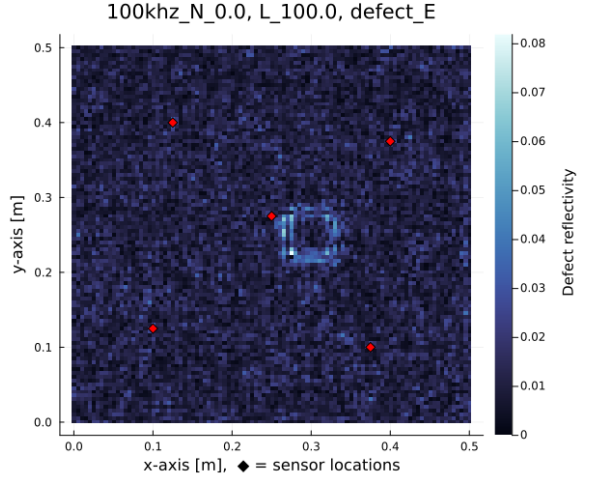


Figure 14: Defect\_A and E reconstructions with  $\lambda = 10.0$ , 5 sensor-emitter configuration. Defect\_A appears rather clearly, while defect\_E is barely visible through the significant background artifacts.

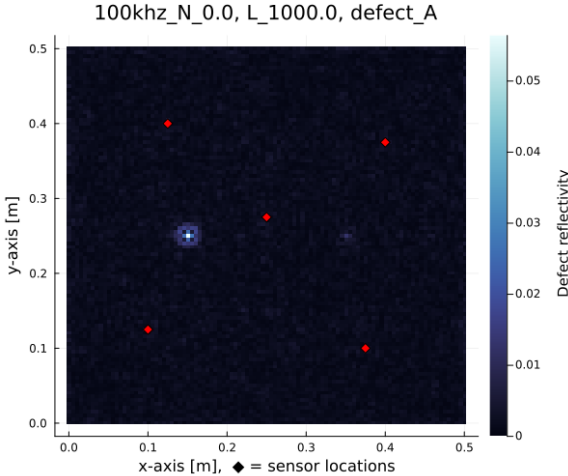


(a) Defect\_A reconstruction.

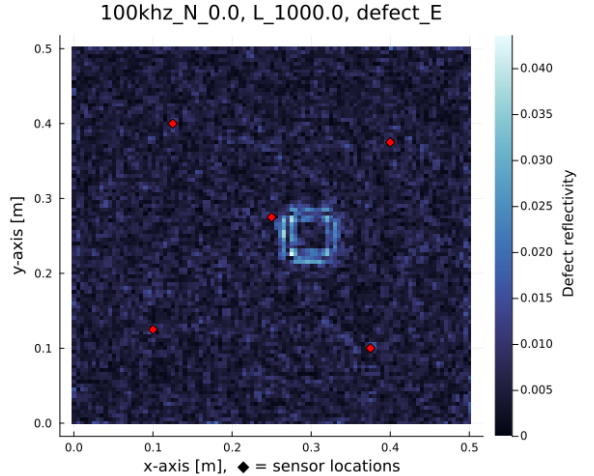


(b) Defect\_E reconstruction.

Figure 15: Defect\_A and E reconstructions with  $\lambda = 100.0$ , 5 sensor-emitter configuration. On both defects, the background artifacts are reduced. Defect\_A looks very similar to the previous figure, but we notice from the colorbar that the amplitudes are roughly 33% lower as a direct result from regularization. Defect\_E is now more clearly visible, with significant reduction in background artifacts.



(a) Defect\_A reconstruction.



(b) Defect\_E reconstruction.

Figure 16: Defect\_A and E reconstructions with  $\lambda = 1000.0$ , 5 sensor-emitter configuration. The shape of Defect\_A now barely changes compared to the previous figure. We note that a small "phantom" defect appearing more clearly mirrored across the y-plane. Defect\_E is now rather clearly visible. Note how the amplitudes of both defects are 50% lower than in the previous figure.

#### 4.2.1 Discussion

These Figures illustrate how increasing the regularization parameter  $\lambda$  affects the defect reconstructions. As  $\lambda$  increases, background artifacts are progressively suppressed. There is a threshold beyond which further increases in  $\lambda$  do not significantly change the shape of the reconstructed defects. This plateauing behavior is typical in Tikhonov regularization [21].

For both defects shown, increasing  $\lambda$  from 100.0 to 1000.0 reduces the amplitude of the reconstructed defects by roughly 50%, with little further reduction in background artifacts. This indicates that the plateau has been reached for both cases. In contrast, when increasing  $\lambda$  from 10.0 to 100.0, the amplitude reduction and artifact suppression are more pronounced, especially for defect\_E. This suggests that the optimal regularization regime is defect-dependent.

The reduction in amplitude with increasing  $\lambda$  is a direct consequence of the regularization term penalizing large solutions. In principle, this amplitude reduction can be predicted and corrected.

An additional observation is the appearance of a "phantom" defect in the reconstruction of defect\_A at high  $\lambda$  (Figure 16a). This artifact is likely due to the poor placement of some sensors. A more detailed discussion and visualization of this symmetry effect and phantom defect seen in Figure 16a can be found in Appendix A.7.

### 4.3 Impact of Noise on Reconstruction

The amount of noise is defined relative to the root-mean-square (rms) amplitude of the first 1 ms of measurement. For example, "10% rms noise" means that the standard deviation of the added noise is 10% of the rms value computed over the initial 1 ms segment of the measured signal. See the code [37] for details.

In order to simulate noise, random noise has been added to the raw simulation data. For all noisy evaluations, 5 sets are data with the added noise are created. These separate noise measurements are crucial for the impulse response computation as done in this thesis (see Section 2.8).

For defect evaluation, the individual measurements were averaged, effectively reducing the noise level compared to the nominal value. The algorithm inherently provides strong noise resistance, as averaging measurements is mathematically equivalent to performing a least-squares fit (see Appendix A.4). Since the amount of measurements can be chosen arbitrarily, this section should be interpreted qualitatively, focusing on observed trends rather than exact quantitative values.

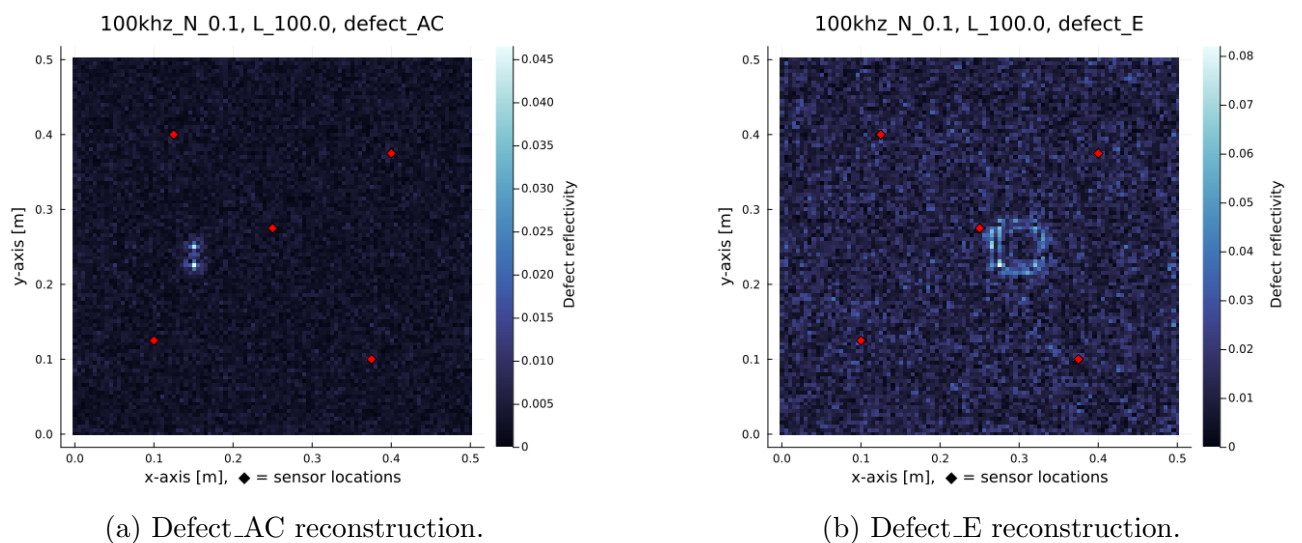
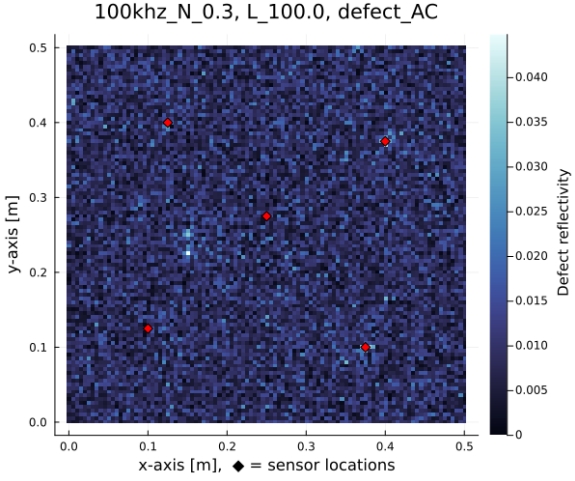
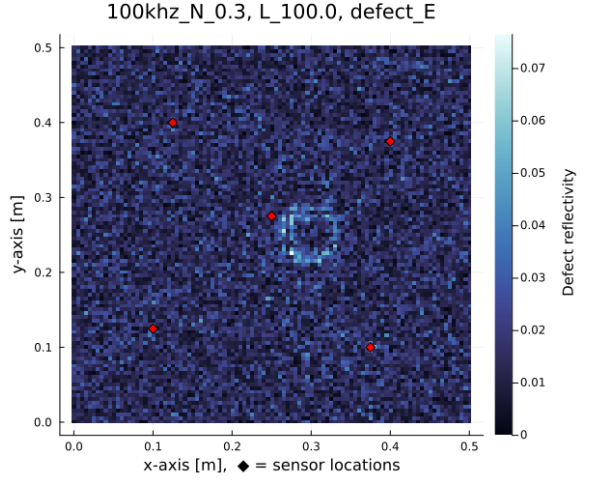


Figure 17: Defect\_AC and E reconstructions at 10% rms noise, with  $\lambda = 100.0$ . The defects are visible, with some background noise artifacts.

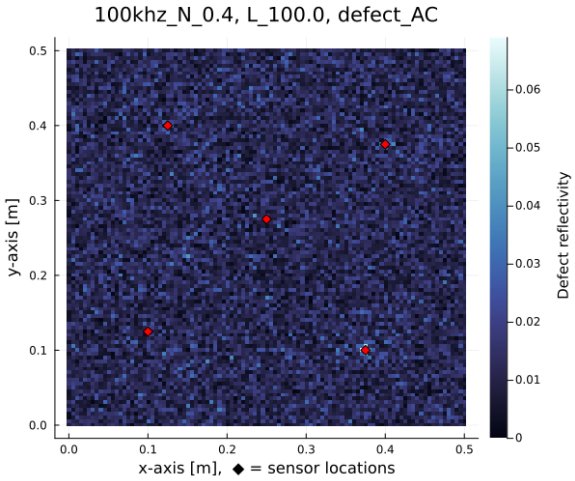


(a) Defect\_AC reconstruction.

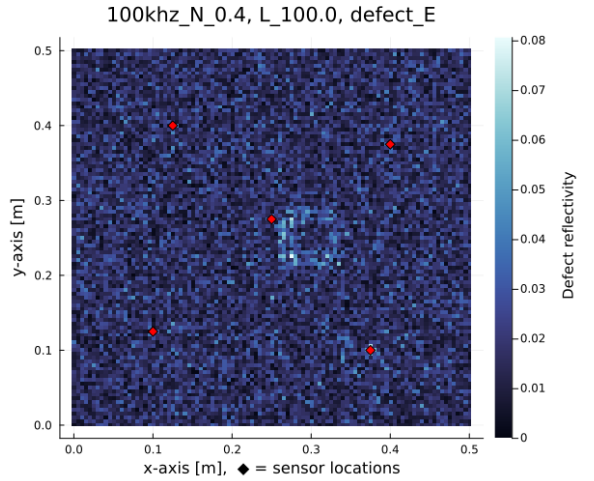


(b) Defect\_E reconstruction.

Figure 18: Defect\_AC and E reconstructions at 30% rms noise, with  $\lambda = 100.0$ . The defects are barely visible, with the background noise approaching the defect amplitudes. The max amplitude seems to decrease by roughly 10% compared to the previous figure, to which I do not have an explanation.



(a) Defect\_AC reconstruction.



(b) Defect\_E reconstruction.

Figure 19: Defect\_AC and E reconstructions at 40% rms noise, with  $\lambda = 100.0$ , 5 sensor-emitter configuration. Defect\_AC is not visible, while defect\_E is barely visible. This is likely a direct result of defect\_E having a larger defect amplitude by default as seen in Figure 17.

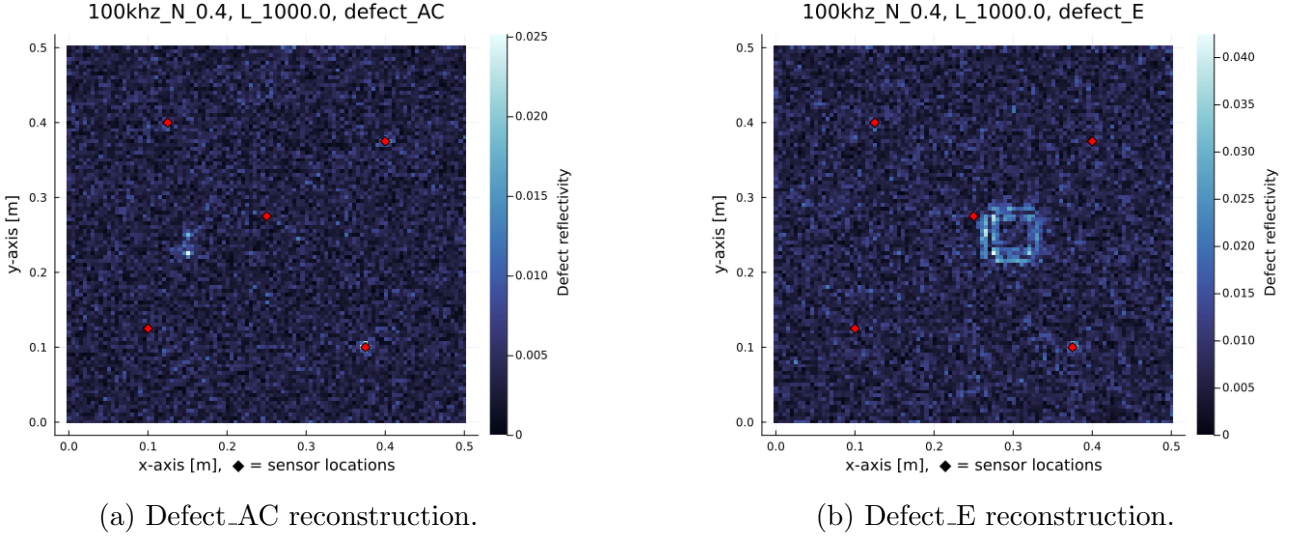


Figure 20: Defect-AC and E reconstructions at 40% rms noise with an increased regularization parameter ( $\lambda = 1000.0$ ), using the 5 sensor-emitter configuration. Compared to the previous figure 19, the higher  $\lambda$  value enhances noise suppression, making both defects visible.

#### 4.3.1 Discussion

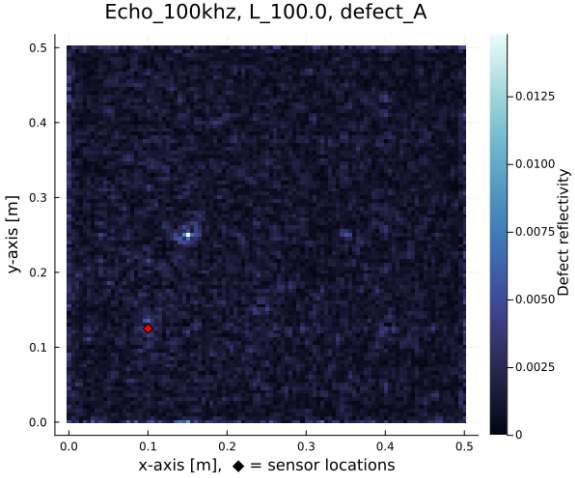
The algorithm exhibits strong noise resistance, remaining effective even with up to 40% rms noise, provided that five repeated measurements are available for each dataset. This is generally feasible, as each measurement period is on the order of milliseconds and the algorithm allows flexible choice of period length (see Section 2.2).

One aspect not fully addressed in the main results is that both the defect data ( $\vec{m}_{\text{full}}$  in equation 34) and the impulse response construction data (Section 2.8) were both considered with the same noise level. This should be considered separately, and has been done in Appendix A.8. As a summary, mostly the impulse response construction is affected by noise.

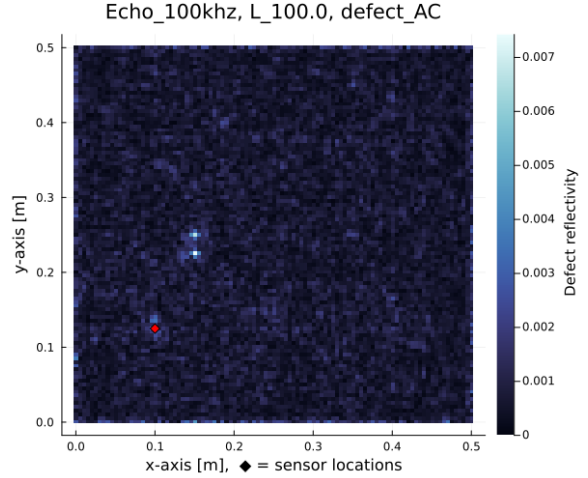
Tikhonov inverted matrices have a very useful property in that the averaging of multiple measurements before multiplying the data with the system matrix is almost equivalent to performing a least squares fit. This is discussed in more detail in Appendix A.4.

### 4.4 Handling Underdetermined Systems with Single Pulse-Echo Reconstruction

In the results so far, 5 sensors have been used, resulting in a system matrix of shape (10'201, 10'000). The system was already slightly underdetermined (by 201 dimensions), but was still capable to reconstructing a variety of defects. To further test the limits, the setup was reduced to a single pulse-echo configuration: only one transducer is present, which emits a pulse and then measures the response at the same location. The resulting system matrix has shape (10'201, 1'000), making it highly under determined. The system matrix is defined as in equation 39.

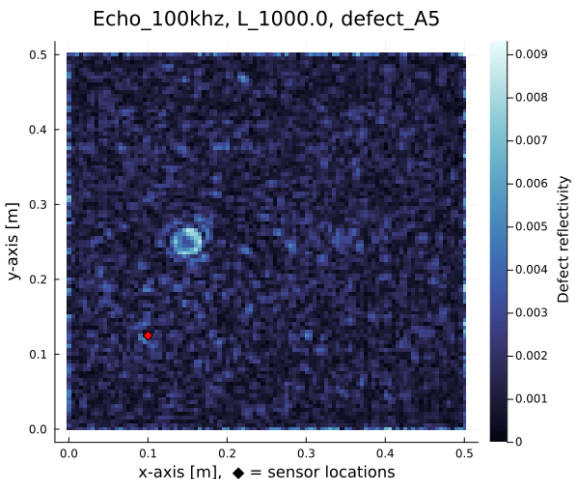


(a) Defect\_A: single emitter, pulse-echo reconstruction.

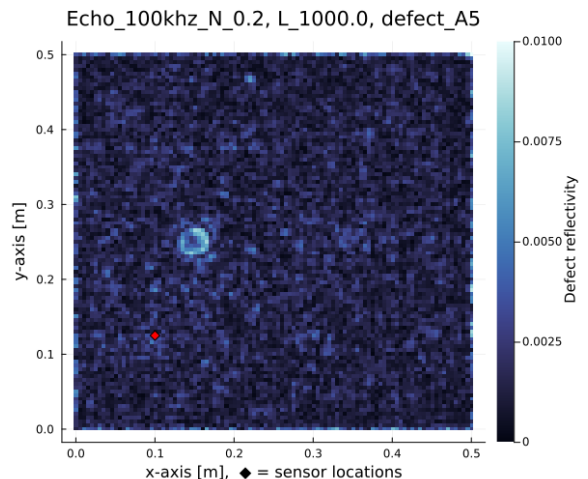


(b) Defect\_AC: single emitter, pulse-echo reconstruction.

Figure 21: Single pulse-echo reconstructions for defects A and AC using only one transducer. The results are comparable to the 5 emitter configurations as in Figures 9, 10.

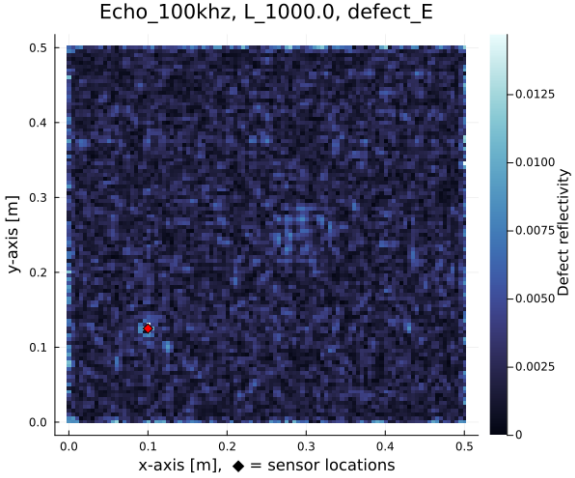


(a) Defect\_A5: single emitter, pulse-echo reconstruction.

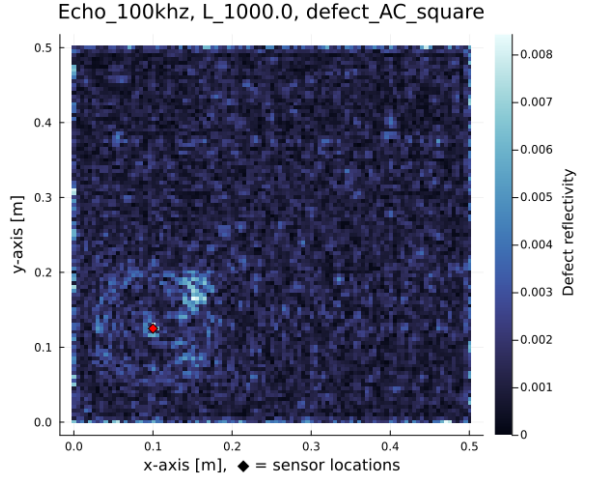


(b) Defect\_A5: single emitter, pulse-echo reconstruction with 20% noise.

Figure 22: Single pulse-echo reconstructions for defect A5 using only one transducer, with and without added noise. The noise resistance appears to be maintained with one transducer only.

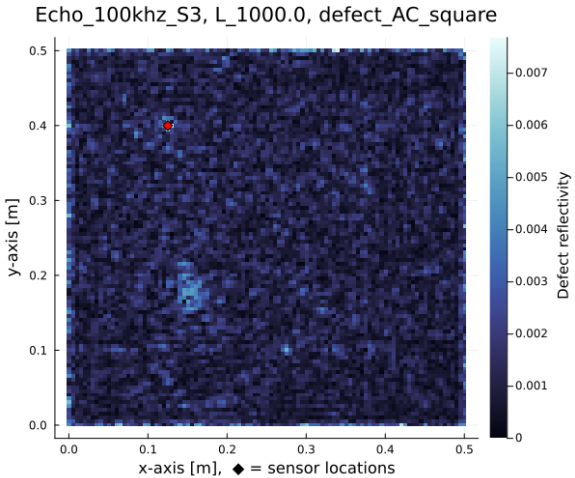


(a) Defect\_E: single emitter, pulse-echo reconstruction.

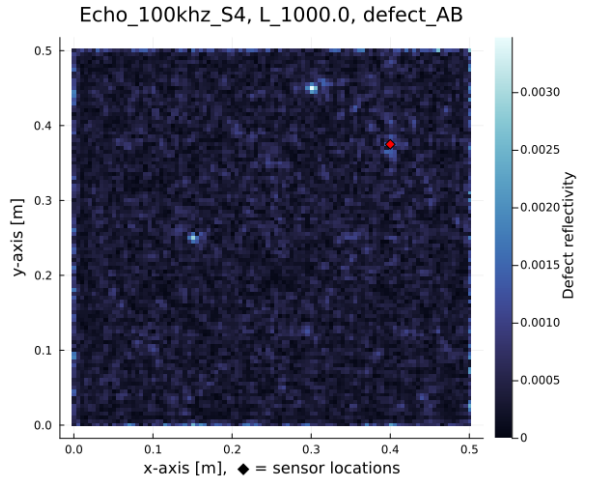


(b) Defect\_AC\_square: single emitter, pulse-echo reconstruction.

Figure 23: Single pulse-echo reconstructions for defects E and AC\_square using only one transducer. The algorithm fails to reconstruct defect\_E, while defect\_AC\_square is reconstructed with halo-like artifacts.



(a) Defect\_AC: single emitter, pulse-echo reconstruction with a different sensor location to previous figures.



(b) Defect\_AB: single emitter, pulse-echo reconstruction with another different sensor location to previous figures.

Figure 24: Single pulse-echo reconstructions for defects E and AC\_square with different locations. Defect\_AC\_square does not show the halo artifact anymore as in Figure 23b. Defect\_AC shows no halo artifact despite having a defect relatively close to the sensor. This defect is documented in appendix A.1

#### 4.4.1 Discussion

A decrease in reconstruction quality is observed, but the performance remains surprisingly robust given that the system is highly underdetermined, using only one-tenth of the data required for a determined solution. The main limitations are seen for defects AC\_square and E, which are the only non-circular defects in this set.

These results demonstrate the algorithm’s ability to exploit edge-induced anisotropy for defect localization, leveraging reflections from plate boundaries. On objects without reflective boundaries, the algorithm cannot resolve the direction of the echo with a single sensor, resulting in halo-like artifacts centered at the sensor location. (See appendix A.9)

The inability to accurately reconstruct defect\_AC\_square in Figure 23b is likely due to its proximity to the single sensor, where boundary effects are insufficient to provide directional information. This is supported by the result for the identical defect in Figure 24a, but with a sensor located further away. However, the susceptibility to this effect appears to depend on the shape of the defect, as Figure 24b shows that a circular defects in proximity to the sensor can still be reconstructed. (This defect is introduced in Appendix A.1). From section 4.1 we know that circular defects are more stable in the reconstruction, which may explain this behavior.

In summary, the algorithm can utilize edge reflection information for localization, but in cases where the defect is less stable, the directional information appears to be removed automatically through regularization.

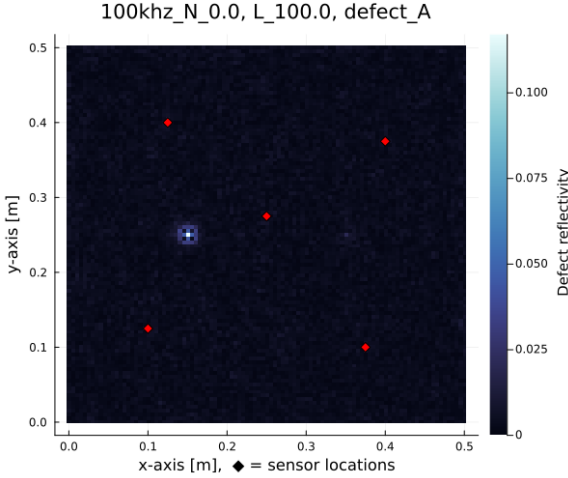
## 4.5 Sub-Wavelength Resolution

This section analyzes the spatial resolution of defect localization as a function of frequency, focusing on the minimum wavelength  $\lambda_{\min}$  estimated from equation 43. Results are grouped by frequency range to highlight differences in reconstruction behavior. A section exploring the importance of sub-wavelength, or sometimes called super-localization can be found in Appendix A.5.

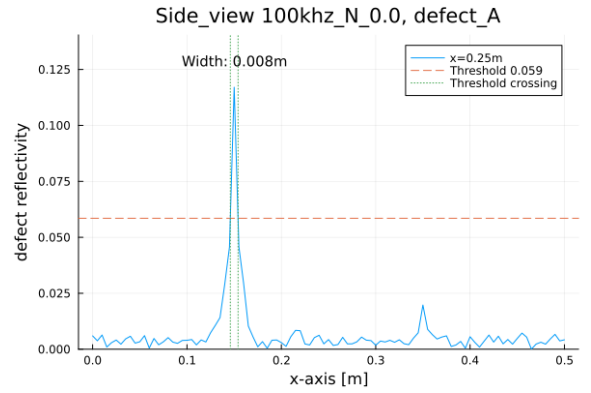
### 4.5.1 100 kHz Range

At a cutoff frequency of 100 kHz, the minimum wavelength is approximately 2.2 cm. The following examples showcase defect reconstructions along with corresponding sideview plots. The sideview plots represent slices of the reconstruction along the x or y-axis. All slices where the half-maximum amplitude is reached are included in the sideview plot. The half-maximum width is then defined as the width of the envelope encompassing all such slices.

**Note:** For larger defects (defect\_A5 and defect\_E), the sideview plots mainly illustrate the overall localization of the shape. While the internal structure of the defect is not resolved in these plots, they still provide useful information about the reconstruction.



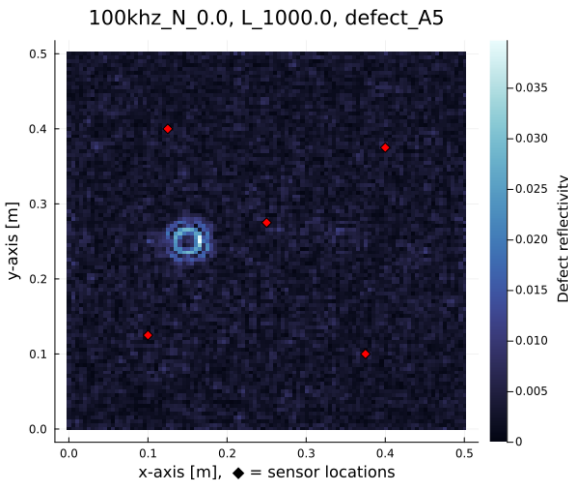
(a) Defect\_A reconstruction,  $\lambda = 100.0$ , 10% rms noise, 5 sensor-emitter configuration.



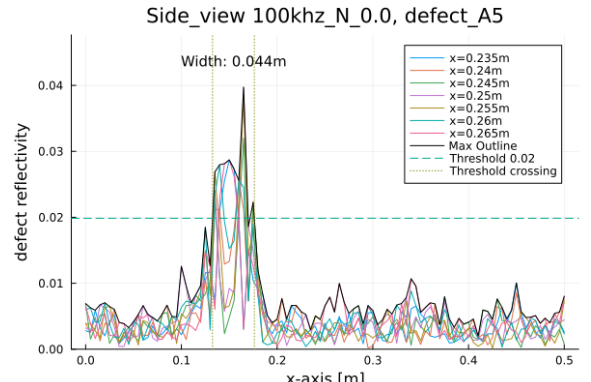
(b) Sideview plot of defect\_A, half-maximum width marked.

Figure 25: Defect\_A reconstruction and sideview plot. The actual defect width is 15 mm, while the reconstructed half-maximum width is 8 mm, significantly below the minimum wavelength.

For larger defects:

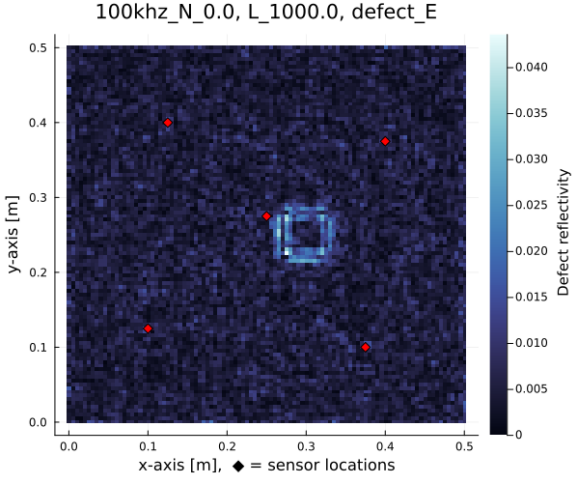


(a) Defect\_A5 reconstruction,  $\lambda = 1000.0$ , 10% rms noise.

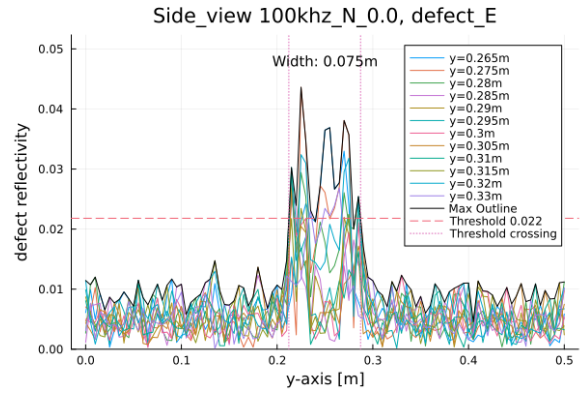


(b) Sideview of defect\_A5.

Figure 26: Defect\_A5 (actual width 5 cm) reconstructed half-maximum width: 4.4 cm, slightly smaller than the true size.



(a) Defect\_E reconstruction,  $\lambda = 1000.0$ , 10% rms noise.

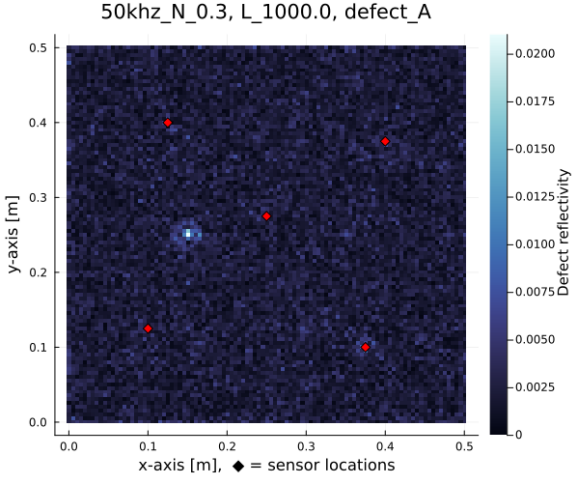


(b) Sideview of defect\_E.

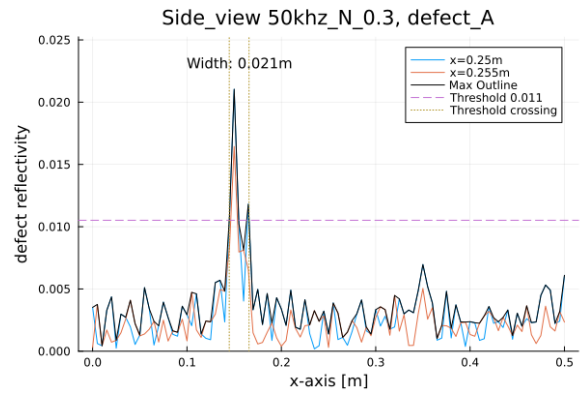
Figure 27: Defect\_E (actual side 5 cm) reconstructed half-maximum width: 7.5 cm, slightly larger than the true size.

#### 4.5.2 50 kHz Range

At 50 kHz,  $\lambda_{\min} \approx 3.5$  cm. Results show that defect widths remain similar to the 100 kHz case, with some increase in background artifacts.

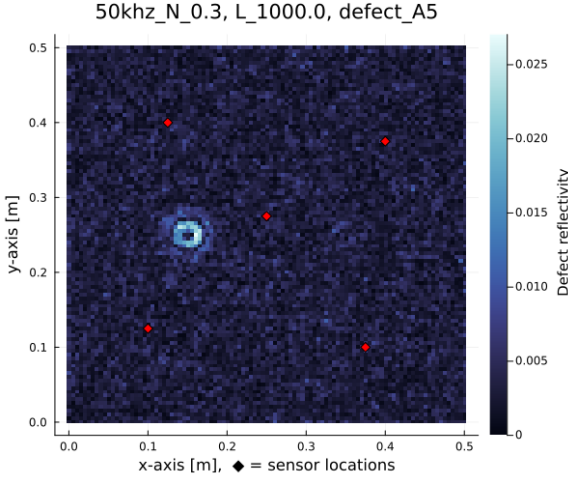


(a) Defect\_A reconstruction,  $\lambda = 1000.0$ , 30% rms noise.

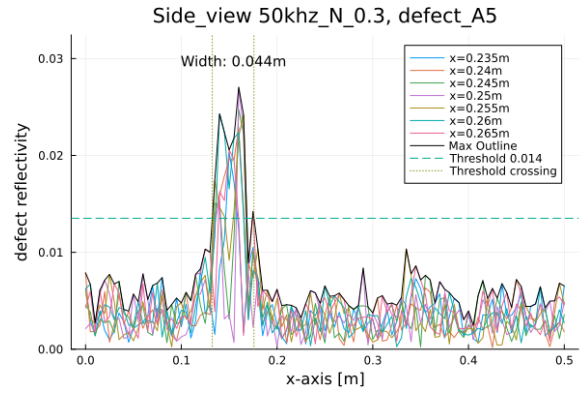


(b) Sideview of defect\_A.

Figure 28: Defect\_A (actual width 15 mm) reconstructed half-maximum width: 2.1 cm.

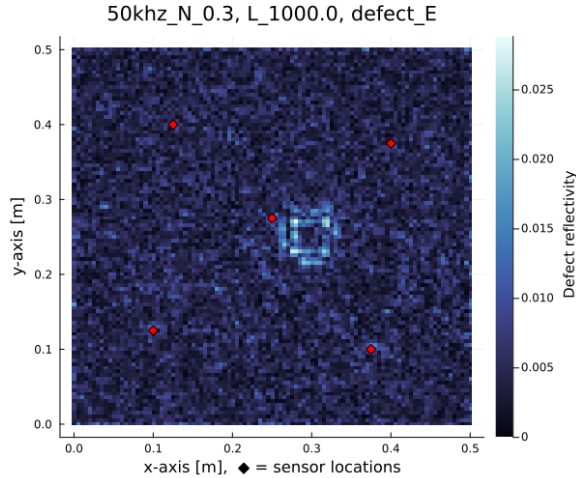


(a) Defect\_A5 reconstruction,  $\lambda = 1000.0$ ,  
30% rms noise.



(b) Sideview of defect\_A5.

Figure 29: Defect\_A5 (actual width 5 cm) reconstructed half-maximum width: 4.4 cm.

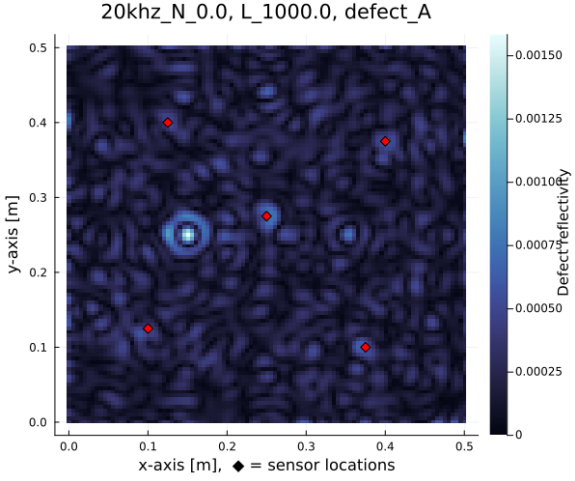


(a) Defect\_E reconstruction,  $\lambda = 1000.0$ , 30%  
rms noise.

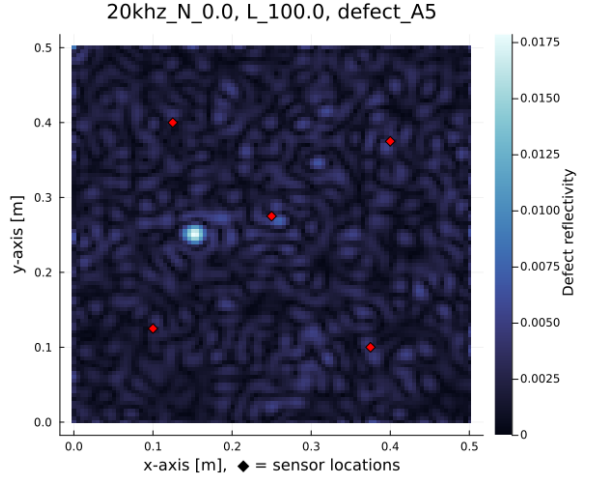
Figure 30: Defect\_E (actual size 5 cm) sideview plot has been omitted due to background noise exceeding half-maximum amplitude.

#### 4.5.3 20 kHz Range

At 20 kHz,  $\lambda_{\min} \approx 6.5$  cm. The system becomes highly underdetermined, and defect shapes are less distinguishable.

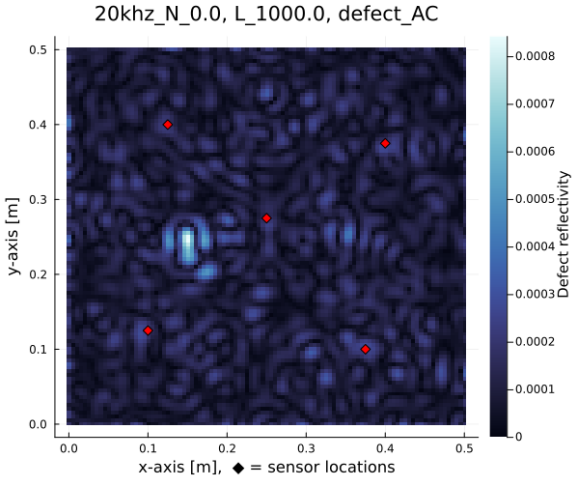


(a) Defect\_A reconstruction,  $\lambda = 1000.0$ , no noise.

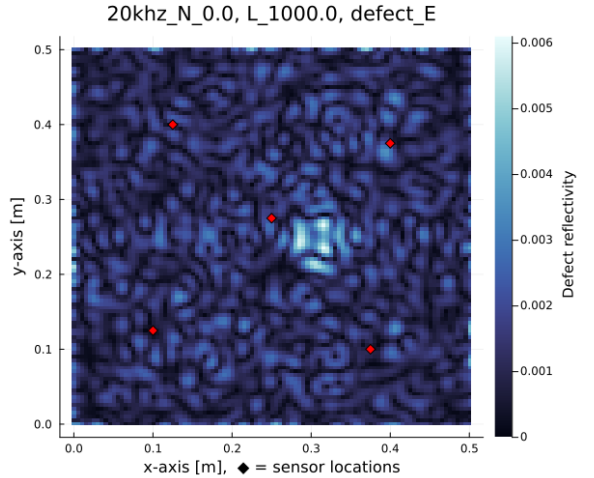


(b) Defect\_A5 reconstruction,  $\lambda = 100.0$ , no noise.

Figure 31: Defect\_A and A5 at 20 kHz. Both defects appear point-like, with widths approximately 5 cm, much smaller than the minimum wavelength.



(a) Defect\_AC reconstruction,  $\lambda = 1000.0$ , no noise.



(b) Defect\_E reconstruction,  $\lambda = 1000.0$ , no noise.

Figure 32: Defect\_AC and E at 20 kHz. Shapes are barely distinguishable, but general sizing is visible.

Sideview plots are omitted due to background noise exceeding half-maximum amplitude.

#### 4.5.4 Discussion

Grouping results by frequency range reveals that the algorithm consistently achieves defect localization below the minimum wavelength, with reconstructed widths often much smaller than  $\lambda_{\min}$ . At higher frequencies, defect shapes are more accurately resolved; at lower frequencies, defects appear with a different, often more soft shape, but the general dimensions are maintained. The spatial resolution decreases, but not at typically expected proportions to the minimum wavelengths (see Appendix A.5).

The low-frequency results are mostly a proof of concept. At these frequencies, the system is highly underdetermined (system matrix size of  $10,201 \times 2,000$  at 20 kHz), so the ability to reconstruct defects is not fully isolated from other factors. For practical implementation at low frequencies, it would be necessary to increase the number of sensors and/or use longer measurement periods to compensate for the reduced information content.

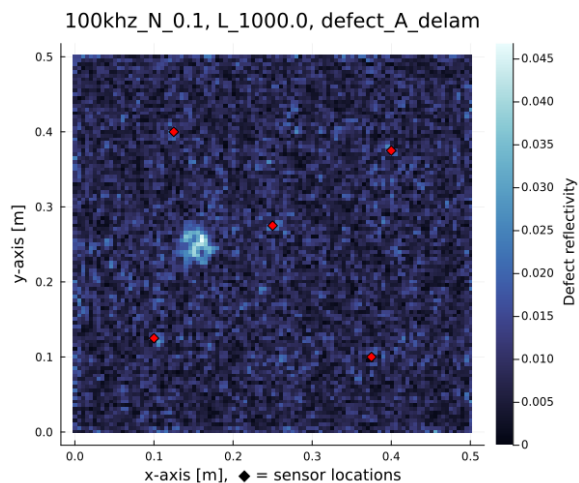
**Remark:** The reconstructed maps indicate effective response amplitudes rather than direct physical properties. At long wavelengths, defects tend to act as point scatterers, and both boundary effects and regularization can influence the apparent size in the reconstruction. For further context, see [31].

## 4.6 Reconstructing Delamination Defects

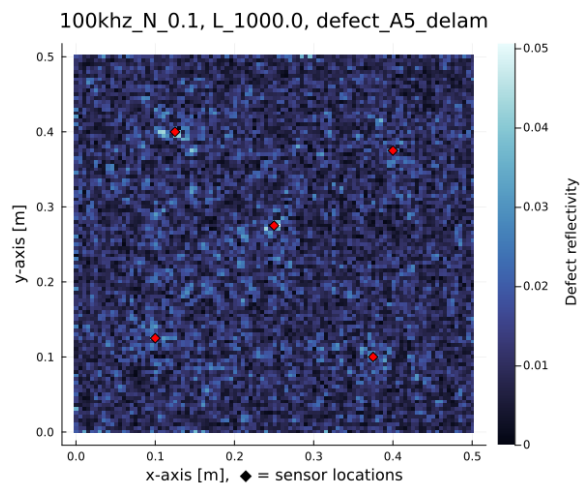
The previously discussed defects all spanned the full plate thickness, effectively acting as holes through the plate. In composite materials, however, delamination, where layers become disconnected—is a more relevant defect type.

To evaluate the algorithm's performance for delamination, two simulations were conducted using the same setup as before, but with defects modeled by disconnecting the mesh within the plate. These defects, labeled "A\_delam" and "A5\_delam," share the same locations and sizes as defects A and A5, but consist of delaminations rather than density changes.

Although the simulations use an aluminum plate, the algorithm does not depend on specific material properties and should be applicable to composites as well.



(a) Reconstructed defect map for delamination defect A\_delam



(b) Reconstructed defect map for delamination defect A5\_delam

### 4.6.1 Discussion

The results show reasonable localization for defect A\_delam (Fig 33a), but poor performance for A5\_delam (Fig 33b). This suggests that the assumption of defects acting as delta pulses is not valid for delamination-type defects. However, this limitation could be addressed by empirically determining the defect response for delaminations, which is feasible with simulation data, as explored deeper in section 6.

Defect A5\_delam also illustrates a scenario where the algorithm fails: the reconstruction is dominated by noise. Observing the amplitudes of the noise by observing the colorbar of figure 33b, being similar to that of figure 33a or many other defects, one may conclude that some defect

must be present. The current implementation does not accurately represent defect amplitudes due to regularization effects, but this could be improved. It is a good property to have that the algorithm when failing does not give a false positive, but rather fills the object with high amplitude noise.

## 4.7 Interpretation and Analysis

The algorithm fundamentally seeks to identify locations where wave reflections occur, which typically correspond to boundaries or interfaces of defects. For defects characterized by density changes, the reconstruction tends to highlight the defect outline, especially for larger defects. However, as defect size decreases, the algorithm increasingly represents them as point-like features. This transition appears to depend on the minimum wavelength used; at sufficiently low frequencies, even defects several centimeters in size are reconstructed as points. Notably, this threshold does not strictly follow the Fourier resolution limit, and sub-wavelength localization is consistently observed. Regularization and noise levels have limited impact on the spatial shape of reconstructed defects.

Overall, the results demonstrate the robustness and adaptability of the proposed algorithm for defect localization, relying solely on empirical data. This makes it suitable for more complex scenarios and materials. Key observations include:

- **Defect Localization Accuracy:** Achieves sub-wavelength resolution with strong noise immunity.
- **Regularization Effects:** The regularization parameter  $\lambda$  controls the trade-off between noise suppression and defect amplitude; moderate values yield balanced results.
- **Noise Robustness:** Maintains reliable reconstructions even at high noise levels; averaging measurements further improves stability.
- **Single Transducer Capability:** Effectively utilizes boundary reflections (anisotropy) to enhance localization.
- **Defect Shape Sensitivity:** Circular defects are reconstructed more reliably than non-circular ones. Different shapes are also well possible. The optimal shape depends on the material isotropy.
- **Underdetermined System Handling:** Tikhonov regularization enables meaningful solutions even when the system is underdetermined.

**Note:** Additional simulations and configurations are discussed in Appendix [A.1](#).

## 5 Conclusion

This thesis presents a linear algebraic framework for inverse wave-based non-destructive testing (NDT), emphasizing a fully vectorized operator formulation. The approach relies on empirically measured impulse responses, enabling defect localization in near arbitrary media. The method circumvents the need for detailed analytical models and is adaptable to various material properties and geometries.

The algorithm demonstrates strong performance in sub-wavelength defect localization, noise resistance, and computational efficiency. The use of Tikhonov regularization stabilizes the inversion, allowing for meaningful reconstructions even in under determined or noisy scenarios.

The framework is general and modular, supporting extensions such as alternative defect bases, regularization strategies, and hardware configurations.

Key takeaways include:

- The method enables sub-wavelength defect localization in simulated aluminum plates and demonstrates strong robustness to measurement noise.
- It operates entirely on empirically measured impulse responses, without requiring assumptions about material properties or geometry.
- The linear algebraic formulation is modular, supporting flexible configurations with arbitrary numbers of sensors and emitters.
- The algorithm is computationally efficient for moderate system sizes, having been implemented fully on a commercial laptop; scaling to larger problems may require further optimization.
- The approach does not depend on precise emitter pulse shapes, provided the pulse remains consistent between calibration and defect measurement.

## 5.1 Comparison with Industry Standard

Compared to the standard C-scan method with roller-based transducers [38, 39, 28], this approach requires a higher initial investment due to the LDV calibration scan. After calibration, defect evaluation is fast and only needs a few installed transducers. The C-scan is more flexible for inspecting varied or changing parts, as it does not depend on permanent sensors or part consistency. In contrast, this method is best suited for repeated testing of consistent components with fixed transducer locations.

There may be a market for this approach in cases where the component is not accessible after assembly, such as internal structures or locations that cannot be reached by hand with a roller. For such scenarios, permanently installed transducers allow for rapid, non-contact defect evaluation without disassembly or physical access, which is not feasible with conventional C-scan methods.

For broader industry use, adapting the calibration step to work with roller-based scanning would reduce costs and improve practicality. Also keep in mind this thesis is only the theoretical framework, and can be adjusted to different measuring devices or hardware configurations.

## 5.2 Comparison with Literature

The Single Pulse Echo Reconstruction from Section 4.4 can be directly compared to the approach in [22]. In that work, the authors localize an active source on a simulated square plate using a single sensor, exploiting edge reflections to improve localization. Their method relies on the plate being flat, rectangular, and isotropic.

As a brief summary, the method in [22] mainly differentiates in relying on an analytical model of Lamb wave propagation in aluminum plates. This thesis relies on an empirical scan instead. Conceptually, the method in comparison used a correlation based approach, in where different propagation paths over edge reflections of the waves are correlated with each other evaluate the agreement of a source being at a certain location. As discussed in Appendix A.5, this approach leads a limit in localization accuracy in relation to wavelength, which is not present in this thesis.

This thesis uses a nearly identical setup: a square aluminum plate with a single emitter sending out a pulse and measuring the echo. The comparison is shown below:

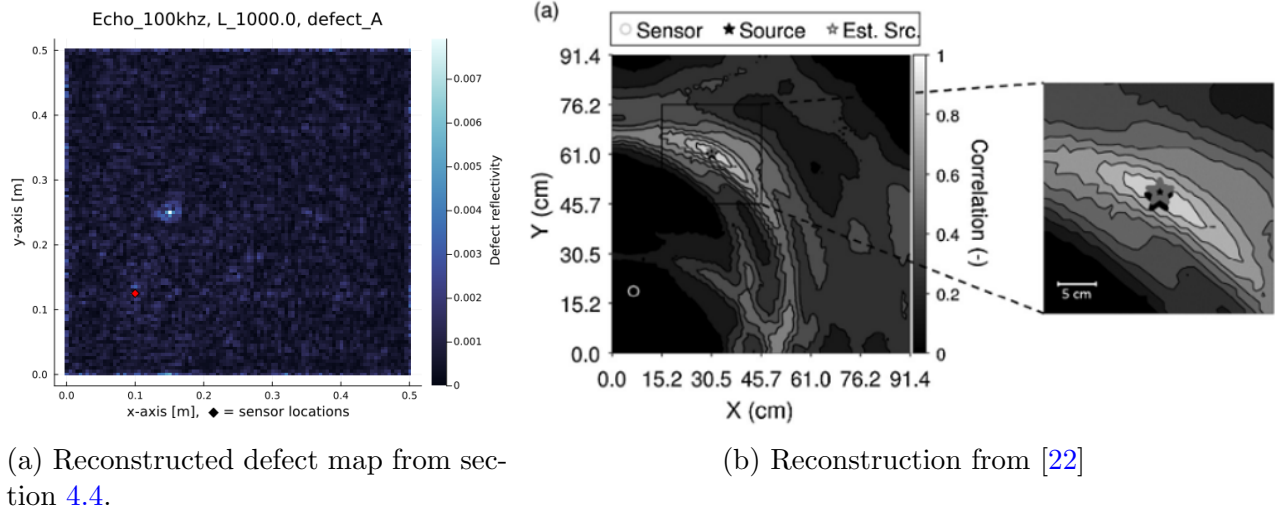


Figure 34: Comparison of single sensor reconstruction: left, this thesis; right, edge reflections paper [22].

The results demonstrate that the proposed method achieves promising localization performance, while not being restricted to rectangular plates, point-like targets, or by the wavelength size in localization accuracy, since it does not rely on correlation-based algorithms. Moreover, it can seamlessly be expanded to multi-sensor and emitter configurations as demonstrated in section 4.

### 5.3 Relation to Signal Theory and Standard Literature

While the physical focus of this thesis is wave-based non-destructive testing, the underlying methodology is fundamentally rooted in signal theory. The approach is built on core concepts such as convolution, impulse response functions, and regularized inversion. These are standard tools in modern signal processing, and the mathematical framework presented here is directly connected to established literature in these fields [35]. While this source can be a good starting point, all methods in the thesis can alternatively be derived manually from foundational concepts in Linear Algebra.

## 6 Future Work

Given the theoretical nature of this thesis, there are many possible directions for future work beyond the initial implementation ideas. The following points are presented in no particular order and are intentionally broad, aimed at readers familiar with the thesis content. For more information on any topic, please feel free to get in touch. Even a brief overview here demonstrates the flexibility and extensibility of the algorithm.

### 6.1 Delaminated defect basis

In section 4.6, the results have been suboptimal. The cause can be traced back to the assumption 4 of section 2.1 being wrong. A better guess for the defect basis is needed, which accounts for delamination-type defects. This can be obtained easily by simulating such a defect, and

essentially solving the defect problem by restricting the defect parameters to the known location of the delamination. One obtains a defect kernel, which describes the re-emission kernel of a delamination. It likely depends on various factors such as depth, material and more, but should not make significant differences for the most part.

I believe there is value in general to know how a delamination responds in this response-formalism.

## 6.2 Combination of multiple pulse sources

This section builds on the concepts introduced in appendix [A.6](#).

Suppose we have two sources,  $\vec{s}_1$  and  $\vec{s}_2$ , located at different grid points. We can impose an artificial reciprocal LTI connection between them by defining  $\vec{s}_2 = g_{12} * \vec{s}_1$ , where  $g_{12}$  could represent, for example, a time delay. This is achieved by calibrating the system with both sources active and the predefined delay, but treating only  $\vec{s}_1$  as the primary source. From the algorithm's perspective, there is simply a strong coupling between source 1 and the location of source 2; it does not distinguish the presence of a second source and treats it as part of the system.

During the measurement step, both sensor locations are recorded, and the measurement at the second sensor is mapped back to the first using the same LTI connection:  $\vec{m}_{total} = g'_{12} * \vec{m}_2 + \vec{m}_1$ , where  $g'$  is the empirically measured impulse response from source 1 to 2, which is not identical to  $g_{12}$  due to wave transfer effects of the object itself.

This approach creates an artificial connection between the two sources, which can be useful for large components where a single source does not provide sufficient coverage, but calibrating multiple sources is impractical.

This is hypothetical and has not been validated yet.

## 6.3 Multi-Component Waves

This section requires the notions introduced in appendix [A.6](#).

In practice, a source emits waves in three spatial directions ( $x, y, z$ ), and each wave component is linearly time-invariant (LTI) connected to the same source term. While the source itself may be split into three components, they are naturally mechanically linked by originating from the same pulse device. This means all measured wave components can be treated together in the same LTI framework, allowing the algorithm to handle multi-component wavefields without additional complexity.

Concretely, I assume that the superposition of all three wave components can be treated as a single linear quantity at each location, after which the same code as in this thesis could be used. I am not fully certain yet about the retaining of reciprocity in doing so, and there may be some rescaling required with the defect measuring data.

This is highly hypothetical and has not been validated yet.

## 6.4 Roller-Based Implementation

The current algorithm is built around using an LDV to perform a full scan of the object, which can be time-consuming and impractical for very large structures such as aircraft hulls.

For industrial viability, a roller-based implementation—similar to established industry methods—would be highly advantageous [38, 39]. In this approach, a sensor would be rolled over the surface to measure responses, but unlike standard techniques, the roller would record signals from fixed emitters installed on the object rather than emitting pulses itself. This would lower the hardware cost significantly.

## 6.5 Averaged objects

In the current implementation, multiple measurements are taken during the calibration step to improve impulse response estimation to reduce noise effects (section 2.8). For serial production components, this approach could be extended to "average" impulse responses across multiple individual objects. In this context, manufacturing inconsistencies act as a form of noise. We essentially obtain an "averaged" model of a set of objects. This could eliminate the need for individual calibration of each object, significantly reducing one of the main limitations of the algorithm.

## 6.6 Generalized Tikhonov Regularization

This thesis employs standard Tikhonov regularization, where the regularization matrix in equation 4 is the identity matrix  $I$  (except the entries that correspond to sensor locations). However, in principle, any regularization matrix can be used; See [6, 34] and related literature for details. I experimented with alternative choices, such as discrete first and second derivative matrices, but observed little impact on the results. While no explicit optimization strategy was found, the use of a default identity matrix suggests there may be room for improvement by exploring more tailored regularization matrices.

## 6.7 Solving for Mounted Parts

Consider a scenario where an object has been calibrated for NDT and subsequently installed in a machine. The mounting points (e.g., bolts or connectors) now act as "defects," absorbing and potentially re-emitting waves with significant time delays. This effect can be addressed by assigning arbitrary defect bases to these locations and excluding them from the final solution, analogous to how transducer locations are handled in this thesis. Specifically, these points are not penalized in the regularization step by appropriately configuring the regularization matrix. This would make the algorithm work without disassembling parts.

## 6.8 Virtual Emitters

Recalling section 2.8, the grid points where the source terms are, are chosen based on where the transducer is placed, however we can abstract the notion of impulse response by simply treating another location to be source location. This would allow one emitter to act as multiple virtual sensors. Such a setup would look like a single transducer which sends out pulses, with multiple "virtual emitters", which would have to be measured using another device such as an LDV. I have tried to implement this in simulation by repurposing the existing code, but it did not yield proper results. This could likely be due to mistakes on my part, as I am quite confident this should work out mathematically.

## 6.9 Multi lambda solutions

Since we require multiple matrices regularized with different  $\lambda$  regularization parameters (see Section 4.2), we can utilize all of them to compare the solutions and filter out background arti-

facts. This is based on the observation that, when multiple  $\lambda$  values yield acceptable solutions, the reconstructed defects remain consistent while the background noise varies with the parameter. This approach is likely more effective when the reflection amplitudes in the reconstruction are not normalized to their absolute values, as done in this thesis. The comparison can be performed using a correlation function between the solutions.

## 6.10 Grid Spacing Optimization

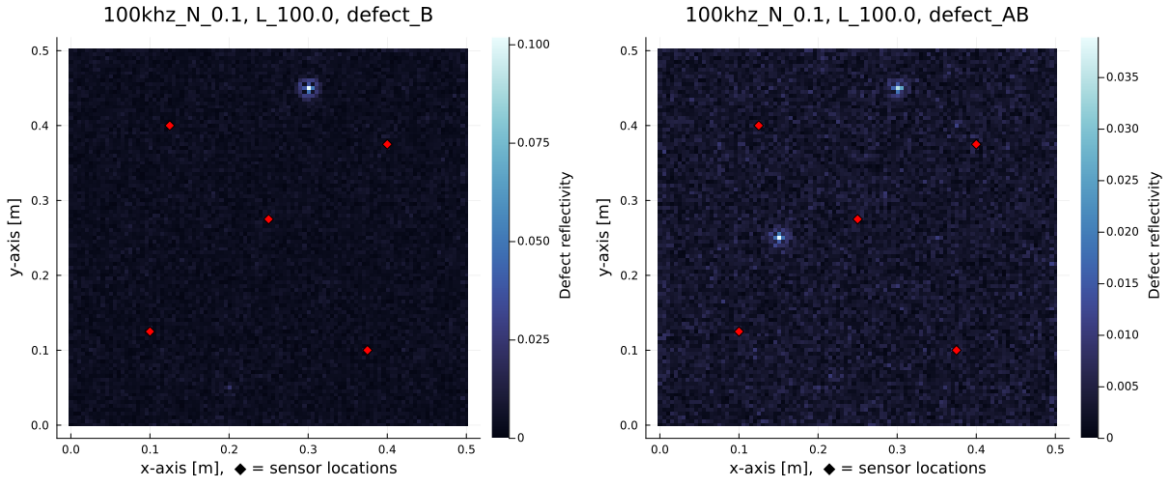
This thesis demonstrates that the algorithm can operate effectively even with relatively low sampling rates, corresponding to long wavelengths. In the current implementation, grid spacing was selected arbitrarily. Increasing the number of grid points raises computational cost, as it expands the defect parameter space and requires more physical measurements.

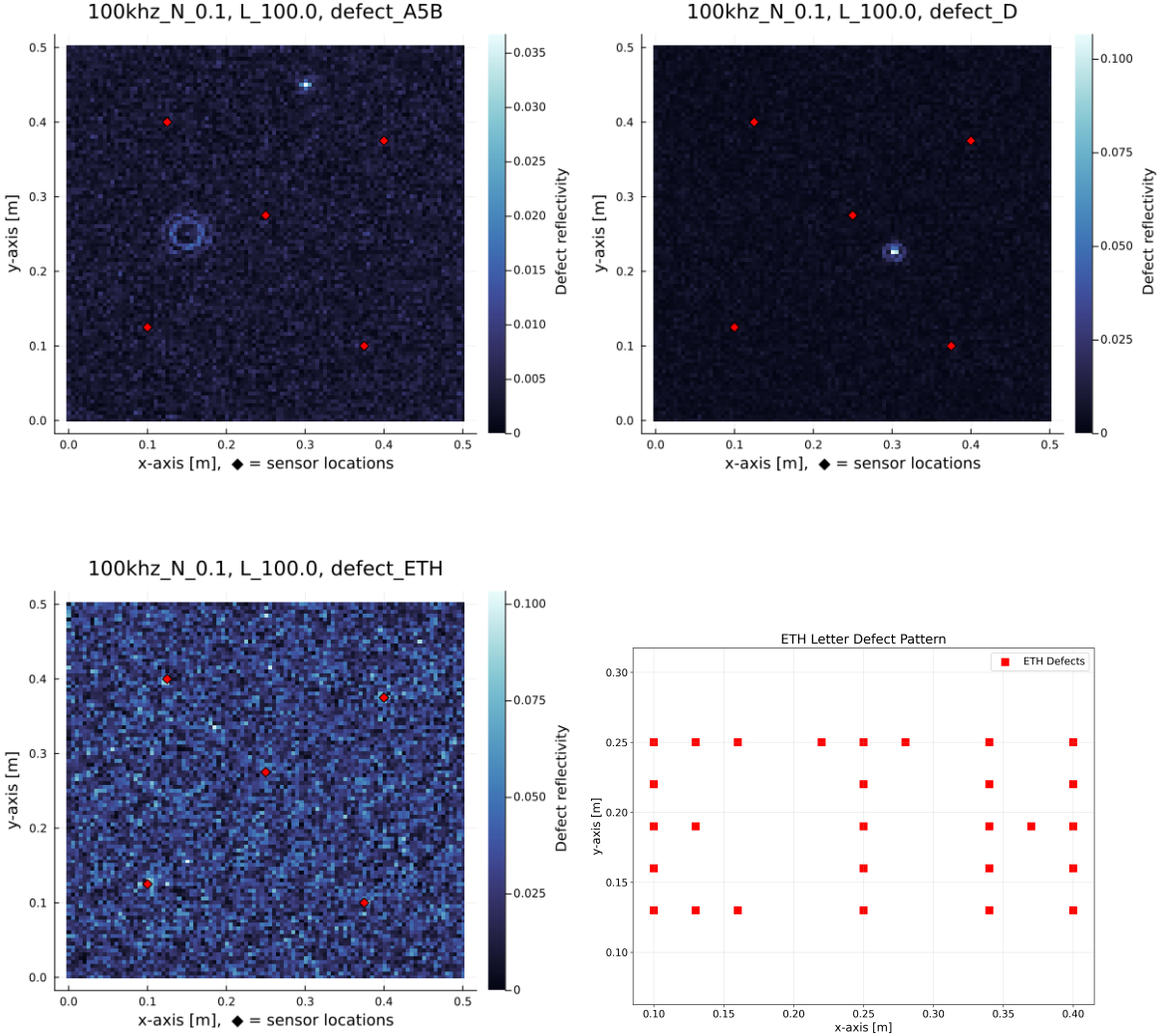
It is likely that the optimal grid spacing is related to the minimum wavelength present in the system, which in this thesis was shown to work with rather long ones due to sub wavelength localization. Establishing guidelines for grid spacing based on wavelength and desired resolution would be valuable, as it could significantly reduce both computational and measurement time. This would enhance the practicality of the approach for larger components.

## A Appendix

### A.1 Additional Defects

More defects have been simulated to test certain properties. Here, a few plots of the results are shown, along with an explanation to what can be learned from them. If one wants to see more results, such as these defects at different frequencies, regularization parameters, or noise levels, they can be found in the GitHub repository [37].





See section 4.1 for images of defects names A, C, A5.

- **Defect B:** A circular defect with same proportions as defect A, but close to the boundary to test the algorithm's ability to localize defects near boundaries.
- **Defect AB:** Defects A and B combined. Similar to defect AC, but tests the ability to localize two defects far apart.
- **Defect A5B:** A combination of defects A5 and B, testing whether the algorithm is capable of localizing two defects of vastly different sizes. There was a fear that the larger defects would dominate the reconstruction, but this does not appear to be the case.
- **Defect D:** An identical defect as A, B, C, but placed between the grid points. The other small defects happened to be places directly over the grid points, and there was a possibility that the algorithm had to rely on this to get the good results.
- **Defect ETH:** A defect meant to push boundaries by writing "ETH" over the entire plate. The letters were composed of square defects which touched to make a block font. This defect appears to be out of the capabilities of the algorithm. It appears that the limits are when a significant part of the object itself becomes part of a defect, however, we did not pinpoint this more accurately.

## A.2 Additional Undocumented Tests

- All simulations documented in this thesis were performed by simulating a 50 kHz Ricker pulse and then lowpass filtering the data to the desired frequency. For low frequencies (e.g., around 20 kHz), the remaining frequency content is minimal, raising concerns that the low frequency solutions may be restricted because of this. Therefore, additional simulations used a 15 kHz Ricker pulse with bandpass filtering to 20 kHz and below. The results were nearly identical, except for minor differences in background patterns, so these were omitted from the main results.
- Increasing the lowpass filter cutoff to 150 kHz had little effect. Bandpass filtering the data from 100 to 150 kHz produced unusable results. Overall, lower frequencies tend to yield more stable reconstructions.
- Defect bases allowing for time delays (i.e., defects re-emitting pulses immediately or with a one-step delay) were tested. These generally acted as smoothing filters on the defect map and did not improve results. This was tried for both multiple emitter systems and single emitter systems, with similar outcomes.
- A defect basis with high and low pass filtered delta pulses as described in equation 22 has been tested. Under ideal conditions, the results were similar to using a regular delta basis, but in highly noisy or unstable situations the solution became more similar to that of low frequency systems such as described in section 4.5, depending on where the lowpass cutoff was set. It appears that by doing this, the solutions internally remove higher frequency parts of the defect basis if these sections are unstable, and can dynamically adjust how high a frequency, and therefore reconstruction resolution it uses.
- The period length was also varied. Simulations typically ran for 10 ms, after which most wave energy had dissipated and the data was treated as periodic. Shortening the period length after simulation showed that the algorithm produced usable results down to about 2 ms, even when half the initial amplitude remained. This suggests the method is tolerant to the degree of wave attenuation before periodicity is imposed. This result is only relevant when simulating the data. In the real world one just repeats the pulses periodically, and therefore the attenuation problem does not apply.
- The same defects, but with a lower change in relative density of 60% instead of 20% were tested, which yielded similar results with less reflective defects.

## A.3 Introduction to Tikhonov Regularization

A concise introduction to Tikhonov regularization can be found in [36] or [6], with the original paper being [8].

The derivation of the Tikhonov inverse is not particularly complex and is often considered standard knowledge in the relevant fields. However, the challenge lies in deriving and understanding the properties of the solution. In this thesis, the Tikhonov inverse is used in a purely applied context, relying on its established properties and practical utility. Similar to how engineers use physics without proving every theorem, the Tikhonov inverse is mathematics applied here based on its known effectiveness, even if not all its theoretical aspects are derived in detail.

Therefore, I will make a quick rundown of the Tikhonov inverse by just stating what it is, with the properties that are relevant for this thesis. Note that this is just the surface of the topic, and the amount of literature exploring other properties is staggering, but not relevant here.

Tikhonov regularization [6], also known as ridge regression, is a widely used method for solving unstable linear inverse problems. It is particularly valuable because it can be applied to any linear system. This section provides a brief overview of Tikhonov regularization.

**Definition 1.** *The right inverse  $M^\dagger$  of an operator  $M$  is defined as the operator satisfying  $M \cdot M^\dagger = I$ , where  $I$  is the identity operator and  $\cdot$  denotes operator composition. It is often referred to as the pseudoinverse.*

This definition originates from general operator theory but is directly applicable to linear systems. For matrices, the operator  $\cdot$  corresponds to matrix multiplication.

The right inverse is a weaker condition than the standard inverse and exists even for non-square matrices. In general, multiple pseudoinverses can exist for a given linear operator. A specific example of a right inverse is the Moore-Penrose pseudoinverse, defined as follows:

**Definition 2.** *The Moore-Penrose pseudoinverse  $M^+$  of a matrix  $M$  is given by:*

$$M^+ := (M^T M)^{-1} M^T, \quad (44)$$

where  $M^T$  is the transpose of  $M$ .

The Moore-Penrose pseudoinverse minimizes the least-squares error of the solution  $\vec{d}$  to the system  $M\vec{d} = \vec{m}$ , i.e., it minimizes  $\|M\vec{d} - \vec{m}\|_2$ . This makes it particularly useful for real-world applications where noise often prevents a perfect solution. In overdetermined systems, it provides the best least-squares fit, while in underdetermined systems, of all possible solutions it selects the solution with the smallest norm, minimizing  $\|\vec{d}\|_2$ .

However, the pseudoinverse is unstable for ill-conditioned matrices, such as the impulse response of a dispersive system. In such cases, the solution becomes highly sensitive to noise, rendering it impractical.

To address this instability, Tikhonov regularization is employed. It generalizes the pseudoinverse as follows:

**Definition 3.** *The Tikhonov regularized inverse  $M^{Tik}(\lambda)$  of a matrix  $M$  is defined as:*

$$M^{Tik}(\lambda) := (M^T M + \lambda \Gamma)^{-1} M^T, \quad (45)$$

where  $\lambda > 0$  is the regularization parameter, and  $\Gamma$  is the regularization matrix, often chosen as the identity matrix.

This inverse minimizes the functional:

$$\|M\vec{d} - \vec{m}\|_2^2 + \lambda \|\Gamma\vec{d}\|_2^2. \quad (46)$$

The regularization term  $\lambda \|\Gamma\vec{d}\|_2^2$  penalizes large solutions. Intuitively, the solution is allowed to deviate from the least-squares solution if the penalty reduced by becoming smaller is sufficiently high. The  $\Gamma$  matrix can be understood to define which quadratic norm the penalty term uses. For example, if  $\Gamma$  is the identity operator,  $\|\Gamma\vec{d}\|_2^2$  is just the standard Euclidean norm. Using this we can penalize derivatives or weigh certain components more than others.

When  $\lambda = 0$ , the Tikhonov inverse reduces to the Moore-Penrose pseudoinverse. The result is a more stable solution that is less sensitive to noise, at the cost of less accuracy.

## A.4 Tikhonov Regularization and Noise

This section demonstrates that averaging repeated measurements is mathematically equivalent to solving a least-squares problem with Tikhonov regularization. In practice, this means that during the measurement step, this algorithm essentially has infinite noise resistance, provided one is willing to average enough measurements.

Suppose we have a system

$$M\vec{d} = \vec{m} \quad (47)$$

and perform  $n$  measurements, yielding vectors  $\vec{m}_1, \vec{m}_2, \dots, \vec{m}_n$ . Stacking these systems gives:

$$\begin{pmatrix} M \\ M \\ \vdots \end{pmatrix} \vec{d} = \begin{pmatrix} \vec{m}_1 \\ \vec{m}_2 \\ \vdots \end{pmatrix} \quad (48)$$

Let  $M_{full}$  denote the stacked system matrix. The Tikhonov inverse for regularization parameter  $\lambda$  is

$$M_{full}^{\text{Tik}}(\lambda) := (M_{full}^T M_{full} + \lambda I)^{-1} M_{full}^T \quad (49)$$

Expanding  $M_{full}$ , we have

$$M_{full}^T M_{full} = nM^T M \quad (50)$$

and

$$M_{full}^T = (M^T \quad M^T \quad \dots) \quad (51)$$

So, equation 49 becomes

$$M_{full}^{\text{Tik}} = (nM^T M + \lambda I)^{-1} (M^T \quad M^T \quad \dots) \quad (52)$$

This can be rewritten as

$$M_{full}^{\text{Tik}} = \frac{1}{n}(M^T M + \frac{\lambda}{n} I)^{-1} (M^T \quad M^T \quad \dots) = (\frac{1}{n}M^{\text{Tik}}(\lambda/n), \quad \frac{1}{n}M^{\text{Tik}}(\lambda/n) \quad \dots) \quad (53)$$

where  $M^{\text{Tik}}(\lambda/n)$  is the Tikhonov inverse with regularization parameter  $\lambda/n$ .

Applying this to the stacked measurement vector yields

$$\vec{d}_{full} = M_{full}^{\text{Tik}} \vec{m}_{full} = M^{\text{Tik}}(\lambda/n) \left( \frac{1}{n} \sum_{i=1}^n \vec{m}_i \right) \quad (54)$$

Therefore, for  $\lambda = 0$  (the pseudoinverse/least-squares case), averaging the measurements and applying the pseudoinverse gives the same result as solving the full stacked system. For  $\lambda > 0$ , averaging the measurements and using Tikhonov regularization with  $\lambda/n$  is nearly equivalent.

In summary, noise resistance is achieved simply by averaging repeated measurements before inversion. This property is especially useful in scenarios with rapid, repeated measurements, as in this thesis.

## A.5 Introduction to Sub-Wavelength Localization

There is significant interest in the algorithm's ability to achieve sub-wavelength localization, as most conventional methods do not offer this capability. Since it is difficult to prove why a method does not fail, the following example is provided to illustrate why other approaches may lack sub-wavelength resolution. While a single example cannot represent all methods, it helps build intuition for the reader to find why it is the case in other methods.

**Setup** Consider a simple 1D scenario: a perfect non-dispersive medium with constant wave speed  $v$ . A pulse  $u(t)$  is band-limited to frequency range  $\Delta f$  (two-sided). A point reflector at position  $x$  produces a two-way delay  $\tau = 2x/v$  in the received signal.

**Time resolution from bandwidth** This is the time-bandwidth (or time-frequency) uncertainty relation, sometimes called the Fourier resolution limit or Rayleigh criterion in signal processing. It expresses the fundamental limit that the duration  $\Delta t$  of a signal and its bandwidth  $\Delta f$  satisfy:

$$\Delta t \gtrsim \frac{1}{\Delta f}.$$

No linear processing can create a narrower main lobe from the same frequency range. Thus, two echoes closer than  $\Delta t$  in time cannot be resolved as separate peaks.

To estimate the location of a reflector, a pulse is emitted, and the echo is recorded. The arrival time is determined by identifying the peak of the echo. There is however a localization uncertainty based to the width of the pulse.

Mapping delay to range uses  $x = \frac{v}{2}t$  (two-way). Therefore, any time uncertainty translates to a spatial uncertainty:

$$\Delta x = \frac{v}{2} \Delta t \gtrsim \frac{v}{2\Delta f}.$$

Thus, converting time resolution to spatial resolution imposes the range localization limit:

$$\Delta x \gtrsim \frac{v}{2\Delta f}$$

In this example, mapping the time-domain pulse onto the spatial domain causes the limitation in localization accuracy relative to the wavelength. In higher dimensions, multiple sensors may be used to triangulate the position of reflectors by back-propagating the received wave in space and cross-correlating the signals. This back-propagation step implicitly maps time to space, resulting in the same limitation.

In contrast, the algorithm presented in this thesis does not use spatial coordinates or wave velocities (Space is arbitrarily indexed with Integers). The algorithm mathematically cannot map time domain pulses to spatial domain due to the lack of information, therefore it never imposes the limitation on itself.

It should be noted that some blurring does occur at very low frequencies, but this is not due to fundamental wavelength limits, rather it is an artifact of Tikhonov regularization. Intuitively, as the grid spacing becomes much smaller than the wavelength, the difference in received signals at neighboring grid points becomes negligible, making it more favorable to spread the solution across multiple points to minimize the total amplitude of the reconstructed defect. A more detailed explanation of this concept can be found in Appendix A.3.

## A.6 LTI systems and impulse responses

We show the following proposition rigorously:

**Proposition.** *For a set of quantities  $\vec{a}_i$  for any  $i$ , which are all LTI related, any linear combination of the  $\vec{a}_i$  are also LTI related.*

This statement is crucial in justifying the use of the generalized linear quantity, which this thesis bases itself on (see section 2.4), and is also required in justifying further future use (sections 6.2, 6.3). This section is not strictly necessary to understand the main thesis.

**Assumption 1.** All quantities in the system are related by a linear time-invariant (LTI) operator  $\mathcal{L}$ .

As an example consider a pulse sent out at location A and measured at location B. The pulse at location A is characterized over time, such as a function  $A(t)$ . If the time is discrete, we instead often describe the pulse as a vector  $\vec{a}$  or  $a^t$ , where instead of a function input  $t$ , we have the indexes of the vector.

In an LTI system, there is a linear operator  $\mathcal{L}$  that connects pulses from A to B. The explicit form of the operator depends on the form of the time domain. The domain may be bounded or unbounded, discrete or continuous. Later on we will be moving into making the time domain periodic and discrete.

The LTI nature of the system restricts the form of the operator  $\mathcal{L}$  to have a symmetry  $\mathcal{L}A(t) = B(t) \implies \mathcal{L}A(t+x) = B(t+x)$  for any  $x$ .

**Assumption 2.** All operators  $\mathcal{L}$  are assumed to be invertible; that is, there exists a unique operator  $\mathcal{L}^{-1}$  such that  $\mathcal{L}^{-1}\mathcal{L} = I$ , where  $I$  is the identity operator.

Equivalently, one can also define that all quantities in the system are uniquely connected by an LTI operator in both directions.

This assumption is semi-empirical in the sense that, it is generally not true. However, in practice we are working with high dimensional vector spaces, where the occasional non-invertability along a single dimension is not relevant.

In the case of a non-invertibility occurring, we make use of pseudo-inverses (aka right inverses), which choose an inverse based on some predefined criteria. The Moore-Penrose pseudoinverse is a famous choice, but we will be using the Tikhonov regularized inverse, which is a generalization of the former.

This will become clear in the following sections, and for now we can just consider this assumption to be a postulate.

**Definition 4.** Quantities are denoted as vectors, e.g.,  $\vec{a}$ .

This hints at later use of discrete, finite vectors, which will lead to matrices as LTI operators. For now  $\vec{a}$  is just a notation.

Technically the LTI relations connect vector spaces instead of individual vectors, but this notation is closer to how the computations are done.

**Definition 5.** Two quantities  $\vec{a}$  and  $\vec{b}$  are said to be uniquely LTI related, if and only if unique LTI operators  $\mathcal{L}_1, \mathcal{L}_2$  exist such that  $\vec{b} = \mathcal{L}_1\vec{a}$  and  $\vec{b} = \mathcal{L}_2\vec{a}$ .

Such a relation is denoted  $\vec{a} \sim \vec{b}$ .

Example: A pulse  $\vec{a}$  sent from location A is measured as  $\vec{b}$  at location B. We can describe the relationship between the two by an LTI operator  $\mathcal{L}$  such that  $\vec{b} = \mathcal{L}\vec{a}$ , for any  $\vec{a}, \vec{b}$ . Since we assume the invertibility of  $\mathcal{L}$  in assumption 2, it follows directly that  $\vec{a} \sim \vec{b}$ .

**Lemma 1.** Transitivity: The relation  $\sim$  is transitive:  $\vec{a} \sim \vec{b} \sim \vec{c} \implies \vec{a} \sim \vec{c}$ .

*Proof.* By definition, the LTI operator from  $\vec{a}$  to  $\vec{c}$  is:

$$\mathcal{L}_{bc}\mathcal{L}_{ab}\vec{a} = \mathcal{L}_{bc}\vec{b} = \vec{c}$$

□

**Lemma 2.** *Reflectivity:* Any quantity  $\vec{a}$  is LTI related to itself, i.e.,  $\vec{a} \sim \vec{a}$ .

*Proof.* The identity operator  $I$  satisfies  $\vec{a} = I\vec{a}$ , thus  $\vec{a} \sim \vec{a}$ .  $\square$

**Lemma 3.** *Symmetry:*  $\vec{a} \sim \vec{b} \implies \vec{b} \sim \vec{a}$

*Proof.* This is equivalent to the invertibility assumption 2. If  $\vec{b} = \mathcal{L}\vec{a}$ , then  $\vec{a} = \mathcal{L}^{-1}\vec{b}$ .  $\square$

These three lemmas show that  $\sim$  is an equivalence relation. However, due to the invertibility assumption not being strictly true, one should take care when using this. Hence, we will not be using general equivalence properties, using the three lemmas individually instead.

**Lemma 4.** *If  $\vec{a} \sim \vec{b}$ , then  $\vec{a} + \vec{b} \sim \vec{a}$  and  $\vec{a} + \vec{b} \sim \vec{b}$ .*

*Proof.* Let  $\mathcal{L}_{ab}$  be the LTI operator mapping  $\vec{a}$  to  $\vec{b}$ .

An LTI relation from  $\vec{a}$  to  $\vec{a} + \vec{b}$  can be constructed as:

$$(I + \mathcal{L}_{ab})\vec{a} = \vec{a} + \vec{b}$$

where  $I$  is the identity operator.

Thus,  $\vec{a} \sim \vec{a} + \vec{b}$ , and due to transitivity,  $\vec{a} + \vec{b} \sim \vec{b}$ .  $\square$

**Lemma 5.** *If  $\vec{a} \sim \vec{b}$ , then  $c_a \cdot \vec{a} \sim c_b \cdot \vec{b}$  for any scalars  $c_a, c_b$ .*

*Proof.* Since  $\vec{b} = \mathcal{L}\vec{a}$ , choosing  $\frac{c_b}{c_a}\mathcal{L}$  as a new LTI operator yields:

$$c_b \cdot \vec{b} = \left( \frac{c_b}{c_a} \mathcal{L} \right) c_a \cdot \vec{a}$$

thus  $c_a \cdot \vec{a} \sim c_b \cdot \vec{b}$ .  $\square$

**Definition 6.** A set of quantities are said to be in an LTI class if and only if all quantities in the set are LTI related to each other.

Due to transitivity, this naturally happens if a path of LTI relations exists between each element of the set. This wording is borrowed from the theory of equivalence classes.

**Proposition 1.** *If  $\vec{a} \sim \vec{b}$ , then any linear combination of  $\vec{a}$  and  $\vec{b}$  are part of the same LTI class.*

*Proof.* By Lemma 5,  $c_1\vec{a}$  and  $c_2\vec{b}$  are part of the same LTI class as  $\vec{a}$  and  $\vec{b}$ . Therefore,  $c_1\vec{a} \sim c_2\vec{b}$ .

Applying Lemma 4 to  $c_1\vec{a}$  and  $c_2\vec{b}$ , we get  $c_1\vec{a} + c_2\vec{b}$  is also part of the same LTI class.  $\square$

**Proposition 2.** *For a set of quantities  $\vec{a}_i$  for any  $i$ , which are all LTI related, any linear combination of the  $\vec{a}_i$  are also LTI related.*

*Proof.* A general linear combination of the  $\vec{a}_i$  can be constructed iteratively by applying Proposition 1 multiple times.

For a desired linear combination  $\sum_i c_i \vec{a}_i$  we can start by individually showing that two elements of the sum are part of the LTI class through Proposition 1. We can then iteratively add the next element by using Proposition 1 on the current sum and the next scaled element.  $\square$

This statement directly justifies why the generalized wave quantity in section 2.4 is valid. Conceptually, when measuring a wave at a single location using an LDV, we are measuring wave components travelling in various directions, as well as a potential source term. Since all wave components are LTI related to the pulse, the superposition of all components (as measured by the LDV) is also LTI related to the pulse. This pulse is moreover LTI related to the superposition of all waves at a different location. Justifying connecting LDV measured quantities with each other through a single LTI operator as it is done in this thesis.

**Note:** There is a need to formally expand this to reciprocal systems, i.e. under what conditions LTI systems retain reciprocity, as this is an assumption which the algorithm makes in section 2.1. So far, it appears that reciprocity is a transitive property, which is retained under superpositions of reciprocal properties, which would be required to justify this thesis fully and future uses (sections 6.2, 6.3).

## A.7 Sensor Symmetry and Phantom Defects

The appearance of phantom defects is closely related to the geometric symmetry of the sensor arrangement. In the case of a rectangular plate with sensors at opposing corners, the system exhibits a 180-degree rotational symmetry about the plate center. If a defect is located on one side of the symmetry axis, the algorithm may reconstruct a mirrored "phantom" defect on the opposite side, particularly when regularization is strong. Figure 38 visualizes this effect.

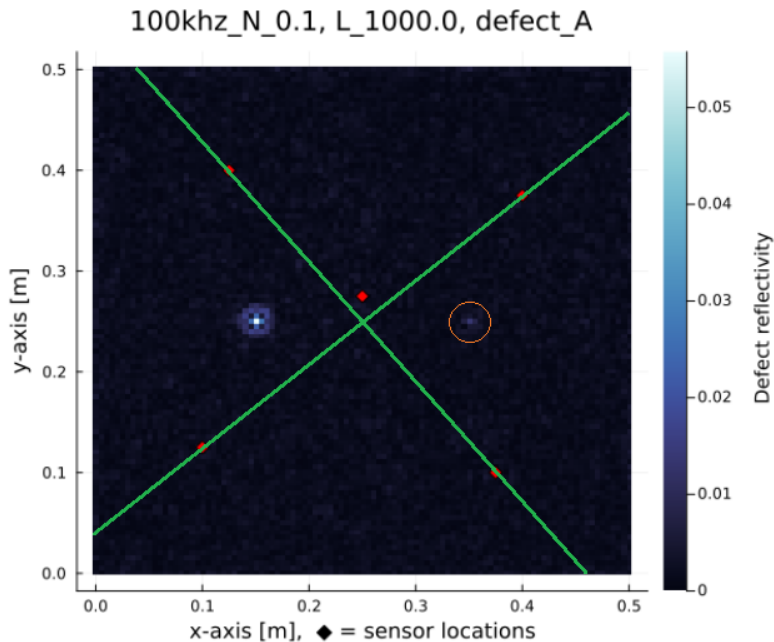


Figure 38: Visualization of symmetry axes defined by opposing sensor pairs (green lines). The orange circular marker indicates the location of a phantom defect, which is the mirror image of a real defect across the symmetry axis. (180-degree rotation).

Even though all sensors together do not have symmetry, just some pairs having symmetry is enough to cause this effect. Since standard Tikhonov regularization uses the  $\ell_2$  norm, it tends to distribute the solution across multiple parameters (e.g.,  $|(2, 0)| > |(1, 1)|$ ). When the algorithm chooses a first location to spread the solutions apart, it prefers locations where fewer sensor pairs disagree. Hence, the appearance of the phantom defect.

This is just a result of poor sensor placement. A general object of arbitrary shape generally

does not have any symmetry axes to account for. Appendix A.9 explores an extreme case of this.

## A.8 Exploring noise resistance separately

In section 4.3, all data measured has been treated equally. An open question remained how much of the errors seen due to noise are associated with impulse response reconstruction, or with the defect measurements. To explore this, two simulations have been made:

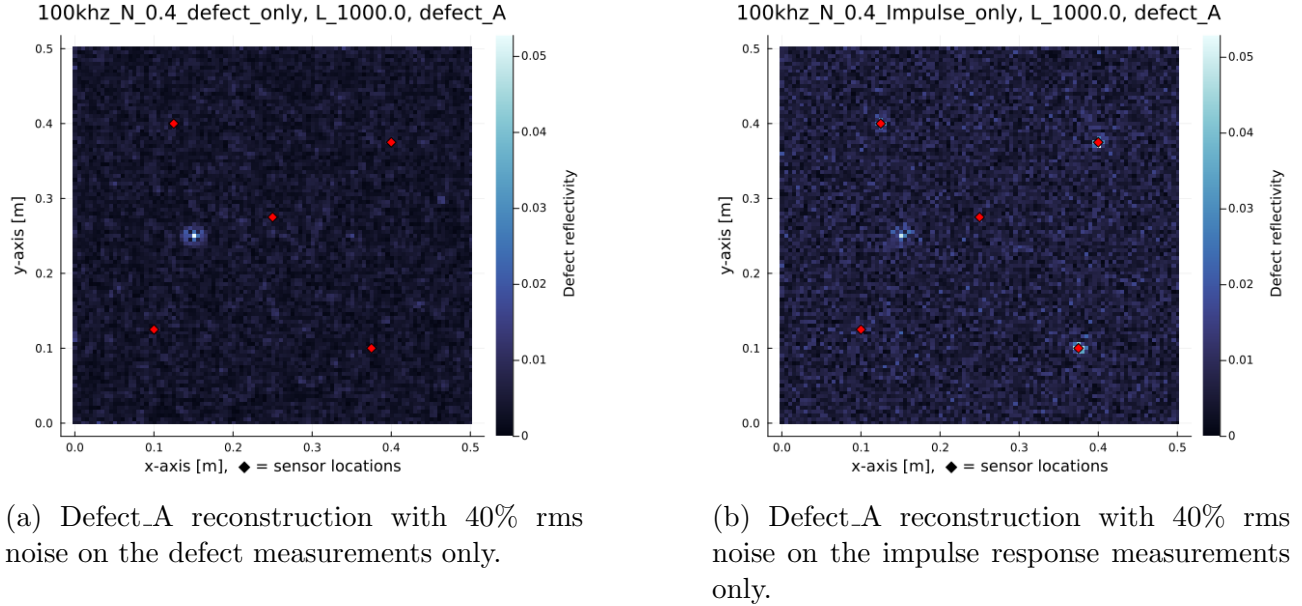
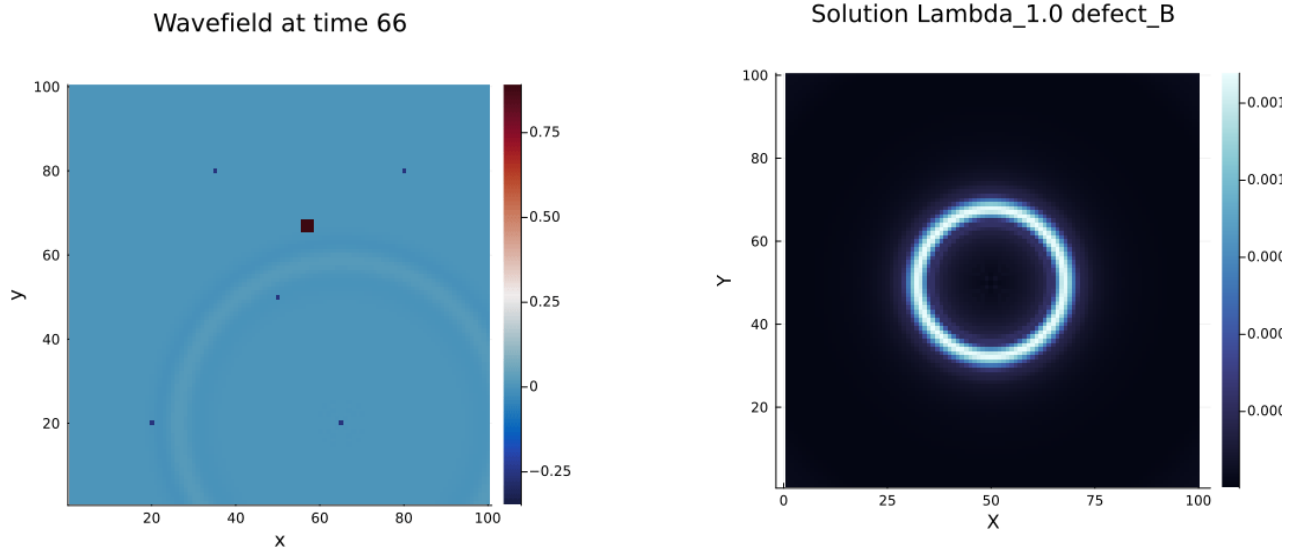


Figure 39: Comparison on the same problem where the noise was applies to either the impulse response or the defect measurements.

The Figures A.8 illustrate that most of the noise is problematic during impulse reconstruction. Taking into account appendix A.4, where we derive that the defect measurement noise is very easily handled by averaging, and defect measurements being much easier to make, it can be safely concluded that the noise is most problematic during impulse response reconstruction.

## A.9 Boundary-less results

Some comments such as in 4.4 note how results would look like without the boundary reflections. A lot of the intuition resulted from some initial experiment using a self written simulation (documented in appendix A.10). Using a single-pulse-echo configuration, we obtain following results:



(a) An image of the self-made simulation, with a square defect. The five sensors can be seen as the dark blue dots. In this snapshot, the bottom right sensor has sent out a pulse.

(b) Pulse-Echo solution where only the center sensor has been used.

Figure 40: Comparison of a self-made boundary less simulation with a square defect (left) and the resulting pulse-echo solution (right).

In Figure 40b, the center sensor emits a pulse and records the resulting echo, resulting in the defect reconstruction as shown. The snapshot in Figure 40a displays all five sensors, with a non-center sensor firing for illustration (which may be confusing). The defect identified in Figure 40b corresponds to the square defect shown in Figure 40a.

As expected, the system cannot distinguish the direction of the echo due to the isotropy of the system, thus we observe a halo around the sensor.

## A.10 Self-Made Simulation

During the initial phase of this thesis, a custom simulation was developed to validate the algorithm before transitioning to commercial software. These results are omitted from the main discussion, as the commercial simulations proved successful and hold more credibility.

The custom simulation is idealized and follows the mathematical formalism used throughout the thesis. It operates entirely in discrete time steps without physical units, focusing on the core algorithmic principles of impulse responses rather than replicating physical wave propagation.

A simplified pseudocode outline is as follows:

```
# Define impulse response vector (e.g., [0, 0, 1, 0.1, 0, ...])
impulse_response = [...]

# Create a square grid (e.g., 100x100)
grid_size = (100, 100)

# Specify source location and pulse
source_location = (x, y)
source_pulse = [...]
```

```

# Fourier transform source and impulse response
source_fft = fft(source_pulse)
impulse_fft = fft(impulse_response)

# Calculate response at each grid point
for x in range(grid_size[0]):
    for y in range(grid_size[1]):
        distance = compute_distance(source_location, (x, y))
        response = impulse_fft .* distance
        result_fft = source_fft .* response
        result = ifft(result_fft)
        # Store or process result

# Define defects as vectors (e.g., [1, 0, 0, 0, ...])
defect_vector = [...]

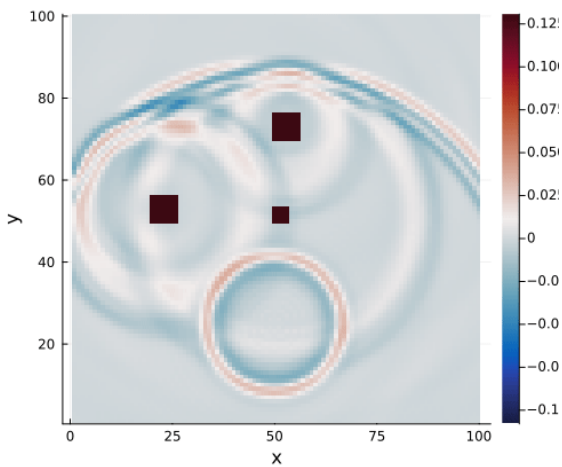
# At each defect location, convolve passing wave with defect vector
for order in target_order:
    for defect_loc in defect_locations:
        passing_wave = get_wave_at_location(defect_loc)
        new_source = convolve(passing_wave, defect_vector)
        # Repeat for desired scattering order (Born approx: order = 1)

```

It provided a controlled environment to test the algorithm's mathematics without concerns about whether the internal model is compatible with actual physics.

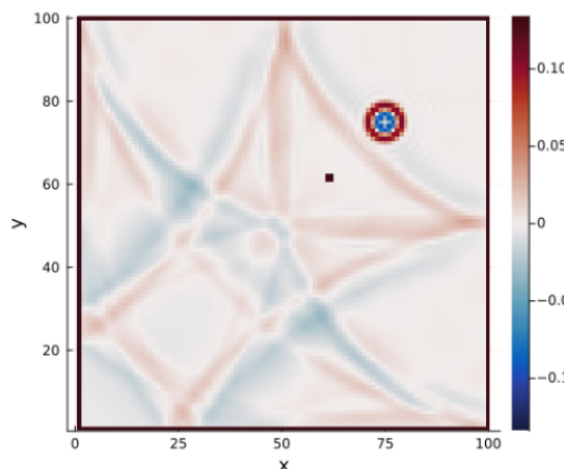
Reflective boundaries can be modeled by placing defects along the object's edges, though selecting appropriate defect vectors is empirical and may require experimentation. This approach is computationally intensive when modeling many reflections, as the computational time scales poorly with increasing amount of defect locations.

Wavefield at time 267



(a) Simulation of higher-order scattering in a boundary-less environment.

Wavefield at time 26



(b) Simulation in a box with reflective boundaries.

Both panels illustrate how pulses from the previous period remain present as new pulses are emitted.

## References

- [1] Yutong Fu, Xuefeng Yao, (2022). A review on manufacturing defects and their detection of fiber reinforced resin matrix composites, Composites Part C: Open Access, Volume 8, 100276, ISSN 2666-6820  
<https://doi.org/10.1016/j.jcomc.2022.100276>
- [2] Muhammad Waqar, Azhar M. Memon, Muhammad Sabih, Luai M. Alhems, (2024). Composite pipelines: Analyzing defects and advancements in non-destructive testing techniques, Engineering Failure Analysis, Volume 157, 107914, ISSN 1350-6307,  
<https://doi.org/10.1016/j.engfailanal.2023.107914>
- [3] Goh Kai Ze, A. Pramanik, A.K. Basak, C. Prakash, S. Shankar, N. Radhika (2023). Challenges associated with drilling of carbon fiber reinforced polymer (CFRP) composites-A review, Composites Part C: Open Access, Volume 11, 100356, ISSN 2666-6820,  
<https://doi.org/10.1016/j.jcomc.2023.100356>
- [4] Yawn, K.R. et al. (1999). Large-Scale Laser Ultrasonic Facility for Aerospace Applications. In: Thompson, D.O., Chimenti, D.E. (eds) Review of Progress in Quantitative Nondestructive Evaluation. Review of Progress in Quantitative Nondestructive Evaluation, vol 18 A. Springer, Boston, MA.  
[https://doi.org/10.1007/978-1-4615-4791-4\\_48](https://doi.org/10.1007/978-1-4615-4791-4_48)
- [5] Derusova, D. A., Vavilov, V. P., Druzhinin, N. V., Shpil'noi, V. Y., Pestryakov, A. N. (2022). Detecting Defects in Composite Polymers by Using 3D Scanning Laser Doppler Vibrometry. Materials, 15(20), 7176.  
<https://doi.org/10.3390/ma15207176>
- [6] Fuhry, M., Reichel, L. (2012). A new Tikhonov regularization method. In: Numer Algor 59, 433–445. Springer, Boston, MA.  
<https://doi.org/10.1007/s11075-011-9498-x>
- [7] Wilcox, P., Monkhouse, R., Lowe, M., Cawley, P. (1998). The Use of Huygens' Principle to Model the Acoustic Field from Interdigital Lamb Wave Transducers. In: Thompson, D.O., Chimenti, D.E. (eds) Review of Progress in Quantitative Nondestructive Evaluation. Springer, Boston, MA.  
[https://doi.org/10.1007/978-1-4615-5339-7\\_118](https://doi.org/10.1007/978-1-4615-5339-7_118)
- [8] Tikhonov, A.N. (1963). On the solution of ill-posed problems and the method of regularization. In: Doklady Akademii Nauk SSSR, 151(3), 501–504.  
<http://mi.mathnet.ru/dan28329>
- [9] Galetti, E., Halliday, D., Curtis, A. (2013). A simple and exact acoustic wavefield modeling code for data processing, imaging, and interferometry applications. GEOPHYSICS, 78: F17-F27.  
<https://doi.org/10.1190/geo2012-0443.1>
- [10] Love, A. E. H. (1888). The Small Free Vibrations and Deformation of a Thin Elastic Shell. In: Philosophical Transactions of the Royal Society of London. A, 179, 491–546.  
<http://www.jstor.org/stable/90527>
- [11] Abrate, S. (2017). Impact on composite plates in contact with water. In: Lopresto, V., Langella, A., Abrate, S. (eds) Dynamic Response and Failure of Composite Materials and Structures. Woodhead Publishing, pp. 183–216.  
<https://doi.org/10.1016/B978-0-08-100887-4.00006-8>

- [12] Ziolkowski, A. (2013). Wiener estimation of the Green's function. In: GEOPHYSICS, 78: W31–W44. Society of Exploration Geophysicists.  
<https://doi.org/10.1190/geo2013-0032.1>
- [13] Kamilov, Ulugbek, Liu, Dehong, Mansour, Hassan, Boufounos, Petros. (2016). A Recursive Born Approach to Nonlinear Inverse Scattering.  
<https://doi.org/10.48550/arXiv.1603.03768>
- [14] Kelvin Koor, Yixian Qiu, Leong Chuan Kwek, Patrick Rebentrost (2023), A short introduction to Wirtinger Calculus with applications in quantum information.  
<https://doi.org/10.48550/arXiv.2312.04858>
- [15] Virieux, J., Operto, S. (2009). An overview of full-waveform inversion in exploration geophysics. In: Geophysics, 74(6), WCC1–WCC26. Society of Exploration Geophysicists.  
<https://doi.org/10.1190/1.3238367>
- [16] Cui, C., Bachmann, E., Peter, D., Liu, Z., Tromp, J. (2023). Source-encoded waveform inversion in the Northern Hemisphere. In: Geophysical Journal International, 235(3), 2305–2322. Oxford University Press.  
<https://doi.org/10.1093/gji/ggad363>
- [17] Rongxin Huang, Zhigang Zhang, Zedong Wu, Zhiyuan Wei, Jiawei Mei, and Ping Wang, (2021), "Full-waveform inversion for full-wavefield imaging: Decades in the making," The Leading Edge 40: 324–334.  
<https://doi.org/10.1190/tle40050324.1>
- [18] Lynda Chehami, Emmanuel Moulin, Julien de Rosny, Claire Prada, Olivier Bou Matar, Farouk Benmeddour, Jamal Assaad, (2014) Detection and localization of a defect in a reverberant plate using acoustic field correlation. J. Appl. Phys. 115 (10): 104901.  
<https://doi.org/10.1063/1.4867522>
- [19] Yasuda, N., Misaki, N., Shimada, Y., Yamaoka, D. (2020). Detection and characteristics estimation of defects in concrete structures using laser ablation-induced vibration. In: Tunnelling and Underground Space Technology, 103, 103460. Elsevier, ISSN 0886-7798.  
<https://doi.org/10.1016/j.tust.2020.103460>
- [20] Scherr, J.F., Kollofrath, J., Popovics, J.S. et al. (2023). Detection of Delaminations in Concrete Plates Using a Laser Ablation Impact Echo Technique. In: J Nondestruct Eval 42, 11. Springer, Boston, MA.  
<https://doi.org/10.1007/s10921-022-00921-x>
- [21] Gerth, D., Ramlau, R. (2021). Estimating Solution Smoothness and Data Noise with Tikhonov Regularization. Numerical Functional Analysis and Optimization, 43(1), 88–115.  
<https://doi.org/10.1080/01630563.2021.2007948>
- [22] Ebrahimkhanlou, A., Salamone, S. (2017). Acoustic emission source localization in thin metallic plates: A single-sensor approach based on multimodal edge reflections. In: Ultrasonics, 78, 134–145. Elsevier, ISSN 0041-624X.  
<https://doi.org/10.1016/j.ultras.2017.03.006>
- [23] Quaegebeur, N., Masson, P., Langlois-Demers, D., Micheau, P. (2011). Dispersion-based imaging for structural health monitoring using sparse and compact arrays. In: Smart Materials and Structures, 20(2), 025005. IOP Publishing.  
<https://doi.org/10.1088/0964-1726/20/2/025005>

- [24] Ji, K., Zhao, P., Zhuo, C., Chen, J., Wang, X., Gao, S., Fu, J. (2022). Ultrasonic full-matrix imaging of curved-surface components. In: Mechanical Systems and Signal Processing, 181, 109522. Elsevier, ISSN 0888-3270.  
<https://doi.org/10.1016/j.ymssp.2022.109522>
- [25] Robert W. Clayton and Robert H. Stolt, (1981), "A Born-WKBJ inversion method for acoustic reflection data," GEOPHYSICS 46: 1559-1567.  
<https://doi.org/10.1190/1.1441162>
- [26] Li, Y., Zhou, Z., Wang, J. (2019). Analysis of Linear Non-Destructive Testing and Evaluation Methods for Thin-Walled Structure Inspection Using Ultrasonic Array. Coatings, 9(2), 146.  
<https://doi.org/10.3390/coatings9020146>
- [27] Hudson, J.A. and Heritage, J.R. (1981), The use of the Born approximation in seismic scattering problems. Geophysical Journal of the Royal Astronomical Society, 66: 221-240.  
<https://doi.org/10.1111/j.1365-246X.1981.tb05954.x>
- [28] Hasiotis, T., Badogiannis, E., Tsouvalis, N. (2011). Application of Ultrasonic C-Scan Techniques for Tracing Defects in Laminated Composite Materials. Strojniški vestnik - Journal of Mechanical Engineering, 57(3), 192-203.  
<http://dx.doi.org/10.5545/sv-jme.2010.170>

#### Non-Paper Sources (Lecture, Tutorial, Reports, Books etc.):

- [29] Jonathan Pillow (2016) Linear Shift-Invariant (LSI) Systems and Convolution  
[https://pillowlab.princeton.edu/teaching/mathtools16/slides/lec22\\_LSIsystems.pdf](https://pillowlab.princeton.edu/teaching/mathtools16/slides/lec22_LSIsystems.pdf)
- [30] A. Muthali et al. (2024) Introduction to Vector Differential Equations  
<https://eecs16b.org/notes/sp24/note8.pdf>
- [31] P. Hermansson, G. Forssell and J. Fagerström (2003) A Review of Models for Scattering from Rough Surfaces  
<https://foi.se/en/foi/reports/report-summary.html?reportNo=FOI-R--0988--SE>
- [32] H.R.Thomsen, et al. (2025) Leveraging guided waves to create digital twins for non-destructive evaluation [Conference presentation]. Measuring by Light 2025, TU Delft, Netherlands.<https://measuringbylight.com/wp-content/uploads/2025/03/V2-Final-Measuring-By-Light-2025-Book-of-Abstracts.pdf> <https://www.mondaic.com/case-studies/non-destructive-testing-using-guided-waves-in-digital-twins-for-cfrp>
- [33] M. I. Skolnik, \*Introduction to Radar Systems\*, 2nd ed., McGraw-Hill, 1980, pp. 3-4, ISBN 0-07-066572-9.
- [34] Per Christian Hansen (2008) Analysis and Solution of Discrete Ill-Posed Problems, pp. 25-33  
<https://www.imm.dtu.dk/~pcha/Regutools/RTv4manual.pdf>
- [35] A.V. Oppenheim, R.W. Schafer (2009) Discrete-Time Signal Processing, 3rd Edition, Prentice Hall 23-35
- [36] Bastian von Harrach (2014) Lecture 2: Tikhonov-Regularization  
[https://www.math.uni-frankfurt.de/~harrach/talks/2014Bangalore\\_Lecture2.pdf](https://www.math.uni-frankfurt.de/~harrach/talks/2014Bangalore_Lecture2.pdf)

[37] GitHub Repository for this thesis

<https://github.com/Fiiidch/Fully-Vectorized-Linear-Operator-Formulation-for-Inverse-S>

[38] Krautkrämer RotoArray compact

[https://www.bakerhughes.com/waygate-technologies/industrial-ultrasonic-testing/portable-ultrasound-equipment/ultrasonic-applications/krautkramer-rotoarray-compact?utm\\_source=chatgpt.com](https://www.bakerhughes.com/waygate-technologies/industrial-ultrasonic-testing/portable-ultrasound-equipment/ultrasonic-applications/krautkramer-rotoarray-compact?utm_source=chatgpt.com)

[39] Phoenix R-Evolution Ultrasonic Array Roller Probe

[https://www.jwjndt.com/product/phoenix-r-evolution-ultrasonic-array-roller-probe/?utm\\_source=chatgpt.com](https://www.jwjndt.com/product/phoenix-r-evolution-ultrasonic-array-roller-probe/?utm_source=chatgpt.com)

[40] Fourier Transform Library FFTW of Julia

<https://www.matecdev.com/posts/julia-fft.html>

[41] Mondaic

<https://www.mondaic.com/>

<https://www.mondaic.com/case-studies/non-destructive-testing-using-guided-waves-in-di>

[42] Lamb wave Dispersion Calculator Python Package

<https://github.com/franciscorotea/Lamb-Wave-Dispersion>